STELLAR POPULATIONS AND STAR FORMATION HISTORY OF THE METAL-POOR DWARF GALAXY DDO 68[*]

E. Sacchi[1,2], F. Annibali[1,2], M. Cignoni[3,4,5], A. Aloisi[3], T. Sohn[3], M. Tosi[2], R. P. van der Marel[3], A. J. Grocholski[6], and B. James[7]

[1] Dipartimento di Fisica e Astronomia, Università degli Studi di Bologna, Viale Berti Pichat 6/2, I-40127 Bologna, Italy; elena.sacchi5@unibo.it
[2] INAF-Osservatorio Astronomico di Bologna, Via Ranzani 1, I-40127 Bologna, Italy
[3] Space Telescope Science Institute, 3700 San Martin Drive, Baltimore, MD 21218, USA
[4] Dipartimento di Fisica, Università di Pisa, Largo Bruno Pontecorvo, 3, I-56127 Pisa, Italy
[5] INFN, Sezione di Pisa, Largo Pontecorvo 3, I-56127 Pisa, Italy
[6] Department of Physics & Astronomy, Louisiana State University, Baton Rouge, LA 70803, USA
[7] Institute of Astronomy, University of Cambridge, Madingley Road, Cambridge, CB3 0HA, UK

ABSTRACT

We present the star formation history (SFH) of the extremely metal-poor dwarf galaxy DDO 68, based on our photometry with the Advanced Camera for Surveys. With a metallicity of only $12 + \log(O/H) = 7.15$ and a very isolated location, DDO 68 is one of the most metal-poor galaxies known. It has been argued that DDO 68 is a young system that started forming stars only ~0.15 Gyr ago. Our data provide a deep and uncontaminated optical color–magnitude diagram (CMD) that allows us to disprove this hypothesis since we find a population of at least ~1 Gyr old stars. The star formation activity has been fairly continuous over all the look-back time. The current rate is quite low, and the highest activity occurred between 10 and 100 Myr ago. The average star formation rate over the whole Hubble time is $\simeq 0.01 \, M_\odot \, \mathrm{yr}^{-1}$, corresponding to a total astrated mass of $\simeq 1.3 \times 10^8 \, M_\odot$. Our photometry allows us to infer the distance from the tip of the red giant branch, $D = 12.08 \pm 0.67$ Mpc; however, to let our synthetic CMD reproduce the observed ones, we need a slightly higher distance, $D = 12.65$ Mpc, or $(m - M)_0 = 30.51$, still inside the errors of the previous determination, and we adopt the latter. DDO 68 shows a very interesting and complex history, with its quite disturbed shape and a long tail, probably due to tidal interactions. The SFH of the tail differs from that of the main body mainly for enhanced activity at recent epochs likely triggered by the interaction.

Key words: galaxies: dwarf – galaxies: evolution – galaxies: individual (DDO 68) – galaxies: irregular – galaxies: starburst – galaxies: stellar content

1. INTRODUCTION

According to hierarchical galaxy formation models, dwarf ($M_\star \lesssim 10^9 \, M_\odot$) galaxies are the first systems to form, providing the building blocks for the formation of more massive systems through continuous merging and accretion. As a consequence, present-day dwarfs may have been sites of the earliest star formation (SF) activity in the universe. On the other hand, in the past, given their high gas content and very blue integrated colors, indicative of the prevalence of young stellar populations, the most metal-poor ($12 + \log(O/H) \lesssim 7.6$, corresponding to $Z \lesssim 1/15 \, Z_\odot$[8]) dwarf irregular (dIrr) and blue compact dwarf (BCD) galaxies have been often suggested to be "primeval" galaxies, experiencing their first burst of star formation, with ages $\lesssim 100$–500 Myr (Izotov & Thuan 1999; Pustilnik et al. 2005, 2008). Only by performing resolved stellar population studies we can properly investigate whether dIrrs/BCDs do indeed host only young stars. All dIrr/BCD galaxies resolved and studied so far with the *Hubble Space Telescope* (*HST*) have been found to harbor stars as old as the look-back time sampled by the depth of the photometry, i.e., ~1 Gyr and older (Tolstoy et al. 1998; Izotov & Thuan 2002; Schulte-Ladbeck et al. 2002; Tolstoy et al. 2009; Tosi 2009). The significance of such studies

is clearly illustrated in the long-standing controversial case of I Zw 18, the most metal-poor prototype of the BCD class with $12 + \log(O/H) = 7.2$ (Skillman & Kennicutt 1993). Imaging with the Advanced Camera for Surveys (ACS) on board *HST* performed by Aloisi et al. (2007) provided a deep and uncontaminated color–magnitude diagram (CMD) that strongly indicated the presence of a previously undetected red giant branch (RGB), thus ruling out its former classification as a truly primordial galaxy (Izotov & Thuan 2004).

Over the past years, several new dIrr/BCDs with extremely low metallicities and physical properties similar to I Zw 18 have been discovered and controversially regarded as "genuine" young galaxies in the nearby universe due to a lack of detailed information on their resolved stellar population ages. One of the most recent cases is Leo P, discovered by Giovanelli et al. (2013) within the ALFALFA survey, with a metallicity from H II region spectra of $12 + \log(O/H) = 7.17 \pm 0.04$ (Skillman et al. 2013). McQuinn et al. (2015) observed it with *HST* and indisputably found RR Lyrae stars, i.e., stars at least 10 Gyr old, from which they also inferred a robust distance estimate of 1.62 ± 0.15 Mpc.

In this paper, we present the interesting case of DDO 68 (UGC 5340), which holds the same record-low metallicity as I Zw 18 and Leo P, $12 + \log(O/H) = 7.15 \pm 0.04$, from long-slit spectroscopy of the ionized gas in its H II regions (Izotov & Thuan 2009). After deriving a distance of 12.74 ± 0.27 Mpc, Cannon et al. (2014) estimated for

---

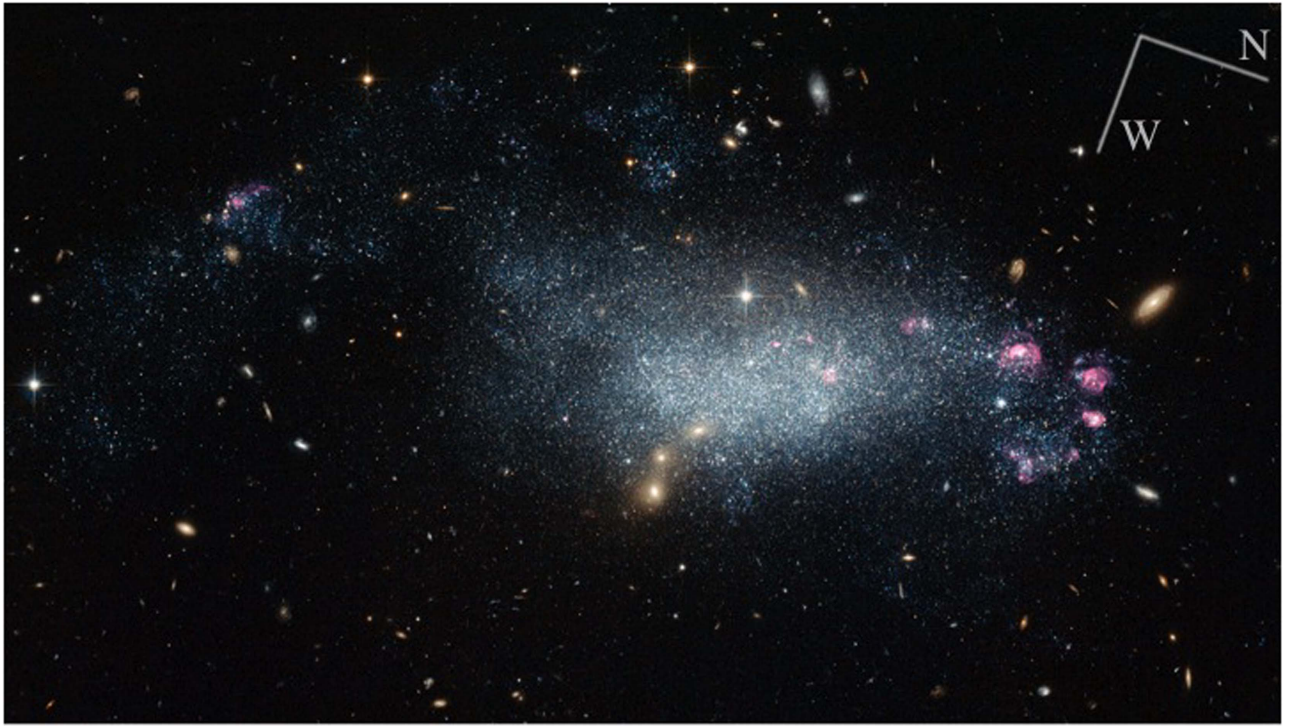[8] Adopting $A(0)_{\mathrm{sun}} = 8.76 \pm 0.07$ from Caffau et al. (2008).

Figure 1. ACS/WFC color-combined image of DDO 68 (blue = broad V, green = I, red = Hα).

DDO 68 a dynamical mass of $M_{\rm dyn} \sim 5.2 \times 10^9 \, M_\odot$ within 11 kpc and an H I mass of $M_{\rm H\,I} = (1.0 \pm 0.15) \times 10^9 \, M_\odot$. Their distance, although larger than the $\sim$9.9 Mpc predicted by its recession velocity ($v = 502 \pm 4 \, {\rm km \, s^{-1}}$), 6.5 Mpc from the apparent magnitudes of the brightest stars (Pustilnik et al. 2005), and 12.0 Mpc derived from the Tip of the Red Giant Branch (TRGB; Tikhonov et al. 2014), places DDO 68 a factor of 1.5 closer than I Zw 18, close enough to resolve its old stars with *HST*.

DDO 68 is especially appealing as a candidate young galaxy because it is located at the periphery of the nearby Lynx-Cancer void (Pustilnik & Tepliakova 2011) and is at least 2 Mpc away from the closest bright galaxies ($L > L_\star$, where $L_\star$ corresponds to $M_B = -19.6$ for $H_0 = 72 \, {\rm km \, s^{-1} \, Mpc^{-1}}$). Within the framework of hierarchical formation scenarios, the evolution of galaxies formed in voids could be quite different than in higher density environments because of a much lower probability of being subject to processes (i.e., encounters and mergers) that are important in shaping and accelerating the evolution of galaxies (Peebles 2001; Gottlöber et al. 2003; Rojas et al. 2004, 2005; Hoeft et al. 2006). As a consequence, some void galaxies may have survived in their nascent state of gaseous protogalaxies until the present epoch and may have just started forming stars as a consequence of a recent disturbance.

DDO 68 presents a very irregular optical morphology, with a long curved tail in the south and a ring-like structure in the northern edge consisting of five separated H II regions (see Figures 1 and 2). The neutral gas morphology and kinematics, as inferred from H I maps by Stil & Israel (2002a, 2002b), are very disturbed as well. DDO 68 is also an outlier of the mass–metallicity relationship (Pustilnik et al. 2005; Berg et al. 2012), being overly massive compared to other systems with comparable metallicity. All these characteristics suggest that DDO 68 may have undergone an

interaction event. However, the closest known neighbor galaxy, the dwarf UGC 5427, is at a projected distance of $\sim$200 kpc. There is no evidence for a physical association between the two galaxies, and, with $M_B = -14.5$, UGC 5427 has a too low mass to have significantly affected DDO 68. So, the absence of an easily identifiable companion to DDO 68 leaves the question of how its recent SF was triggered open. From the analysis of the spatial distribution of stars resolved in *HST*/ACS imaging, Tikhonov et al. (2014) argued that DDO 68 in fact consists of two different systems: a central most massive body and an elongated arc-shaped body (DDO 68 B). In a recent work based on Very Large Array observations, Cannon et al. (2014) claimed to have found an object with the same systemic velocity of DDO 68. This gas-rich galaxy (DDO 68 C) has a total neutral hydrogen mass of $M_{\rm H\,I} = (2.8 \pm 0.5) \times 10^7 \, M_\odot$ and lies at a distance of $\sim$42 kpc from DDO 68. The detection of a bridge of low surface brightness gas connecting DDO 68 and DDO 68 C may suggest an interaction between the two objects.

In this paper, we present the star formation history (SFH) of DDO 68 based on deep *HST*/ACS data. The derived CMD, which reaches down to $\sim$1 mag below the TRGB, implies that DDO 68 started its star formation at least $\sim$1–2 Gyr ago (and possibly up to a whole Hubble time) disproving the hypothesis that it is a truly primeval galaxy of recent formation. We analyzed the populations of stars resolved with *HST* in and around DDO 68 and applied the synthetic CMD method (Tosi et al. 1991) to infer its SFH. We also provide a new distance estimate, based both on the TRGB and on the whole CMD fitting.

2. OBSERVATIONS AND DATA REDUCTION

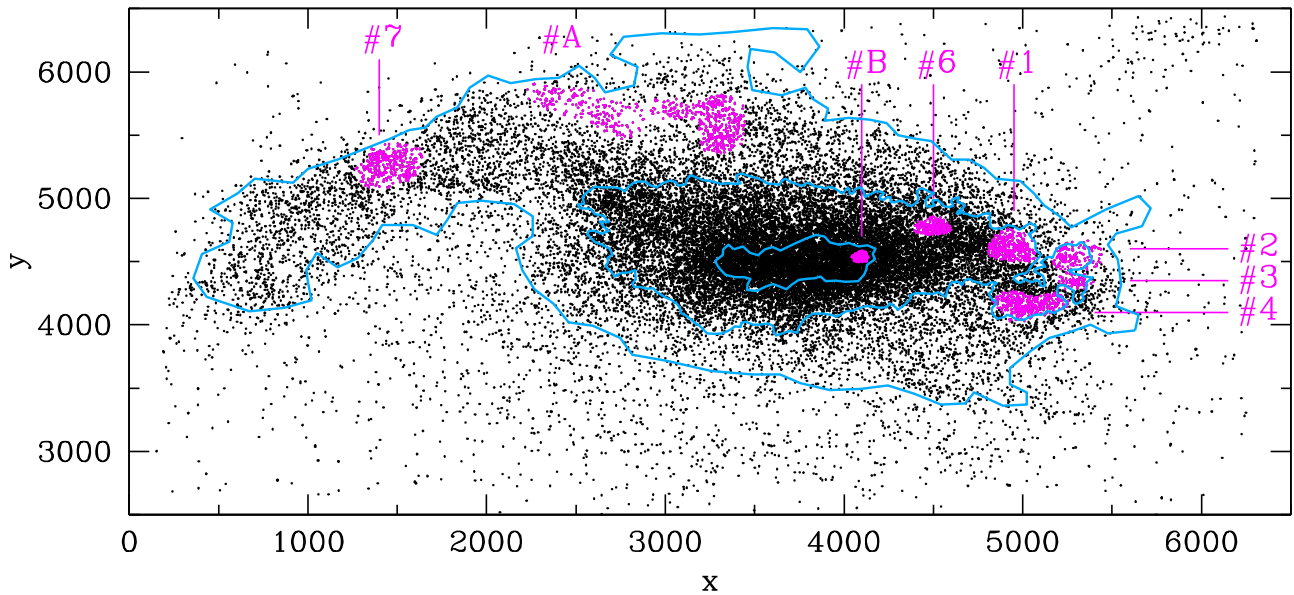Deep imaging with the ACS Wide Field Channel (WFC) of DDO 68 was performed on 2010 April 27 and May 2 (GO

Figure 2. Map of the stars with the isophotal contours superimposed (light blue lines), which were used to identify the four regions for the analysis of the galaxy SFH. Region 1 is the most central one, and Regions 2, 3, and 4 are increasingly more external. The magenta points are the stars within the H II regions labeled as in Pustilnik et al. (2005) and Izotov & Thuan (2009) except for A and B, which they do not take into account in their analysis.

program 11578; PI Aloisi) using the F606W (∼broad V) and F814W (∼I) broadband filters and the F658N (Hα) narrow band filter. The total integration time is ∼2400 s in F658N, and ∼6940 s in both F606W and F814W. In addition, coordinated observations were made in parallel with the UV-optical channel (UVIS) of the Wide Field Camera 3 (WFC3), in both F606W and F814W filters. The results from the latter are not discussed here and will be presented in a subsequent publication.

We have observed DDO 68 with a standard dither pattern in both filters to fill the gap between the two CCDs of the ACS and improve the sampling of the point-spread function (PSF). All images were processed with the latest version of CALACS, the ACS pipeline. We applied to them the whole routine developed by Anderson & Bedin (2010) to correct for Charge Transfer Efficiency. Eventually, we combined all the images in the same filter into a single frame using the MULTIDRIZZLE software package (Fruchter et al. 2009). MULTIDRIZZLE allows us to fine-tune the alignment of the images, correct for small shifts, rotations, and geometric distortions between the images, and remove cosmic rays and bad pixels. The final V and I images were eventually resampled to a pixel size of 0.033 arcsec (0.68 times the original ACS-WFC pixel size). Figure 1 shows a three-color-combined image of DDO 68.

We have performed PSF-fitting photometry on the V- and I-band images using the stand-alone versions of DAOPHOT and ALLSTAR (Stetson 1987). To create the PSF models, we selected ∼174 and ∼265 bright, relatively isolated stars in V and I, respectively, with good spatial coverage across the entire image. The PSF was modeled with analytic MOFFAT (F606W) and PENNY (F814W) functions plus second-order additive corrections as a function of position derived from the residuals of the fit to the PSF stars. Next, we ran ALLSTAR to fit the PSF models to the sources detected independently in the V and I images. To push the photometry as deep as possible, we repeated the procedure on the subtracted images, allowing for the detection of faint companions near brighter stars. The V and I catalogs were finally cross-correlated adopting a matching

radius of 1 pixel, providing a final matched catalog of ∼35,000 objects.

The calibration of the instrumental magnitudes into the *HST* VEGAMAG system was performed by applying the Bohlin (2012) time-dependent ACS zero points provided by STScI.[9] To determine the aperture corrections to the conventional 0″5 radius aperture, we performed photometry on several bright and isolated stars in our images. The correction from 0″5 to an infinite aperture was done using the old Sirianni et al. (2005) values instead.[10]

In order to clean the photometric catalog from spurious objects, we applied selection cuts on the DAOPHOT parameters σ (photometric error), χ^2, and sharpness, as shown in Figure 3: to retain a star, we required that $\sigma_V < 0.3$, $\sigma_I < 0.3$, sharp$_V > -0.5$, and sharp$_I > -0.5$. Furthermore, we applied an additional cut in sharpness and χ^2 following the upper envelopes of the distributions (see Figure 3).

A visual inspection in the images of the rejected objects, coupled with an analysis of their radial profiles, revealed that the majority of them are background galaxies, unresolved stellar clusters, or blends of two or more stars. The same inspection was performed for objects brighter than ∼23 mag in V or I, independently of their χ^2 and sharpness. After these selections, we were left with ∼30,000 objects.

3. INCOMPLETENESS AND ERRORS

Incompleteness and errors of our photometry have been evaluated performing artificial star tests on the images. To this aim, we added artificial stars created with the adopted PSF to the images and exploited the DAOPHOT/ADDSTAR routine, which simulates real stars adding the appropriate Poisson noise to the artificial stars, and allows us to cover the desired range of

---

[9] http://www.stsci.edu/hst/acs/analysis/zeropoints

[10] According to Bohlin (2012) the new Encircled Energy values are within 1%–2% of the corresponding Sirianni et al. (2005) results; therefore, we expect a negligible effect on our photometry, also considering the typical size of the photometric errors.
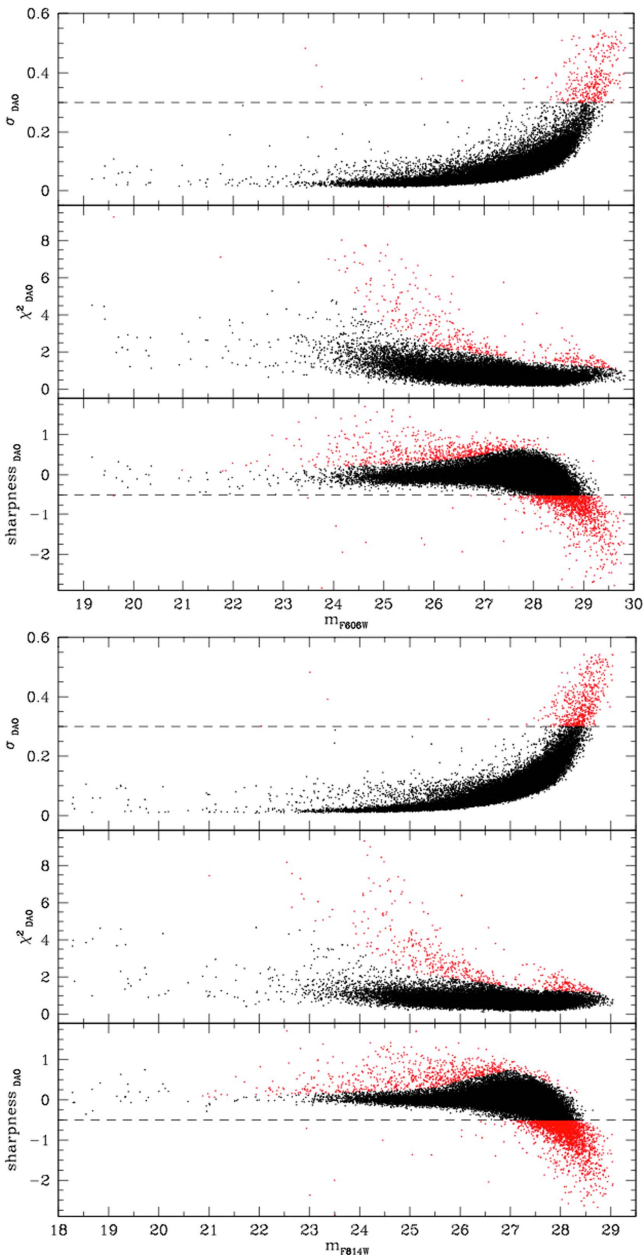
Figure 3. Selection cuts applied to the photometric error σ_{DAO} (top panels), χ^2 (middle panels), and sharpness (bottom panels) for the two filters. The red and black points are, respectively, the discarded and the retained objects.

positions and magnitudes. The range of magnitudes covered by the artificial stars was chosen to match the data. We divided the images into grids of 30×30 pixel^2 cells and placed one artificial star in each cell at each run, to efficiently compute the completeness without altering the crowding on the images. To avoid overcrowding, we also imposed that no two artificial stars laid within 20 pixels of each other, since the PSF radius is 15 pixels. The images were fully sampled because we let the starting position of the grid and the position of the artificial star within each cell vary appropriately. We performed PSF-fitting photometry of the images with the added artificial stars with the same procedure as for the real data described in Section 2. We then cross-correlated stars in this output catalog with those in the combined catalog that includes both the original photometric catalog and the input artificial star catalog. An input

artificial star was considered "lost" when it was not recovered in the output catalog, or when its recovered magnitude differed from the input value by more than 0.75 mag. We then cleaned the artificial star catalog applying the same criteria in photometric error, χ^2, and sharpness used in the real data. In total, we simulated $\sim 1,800,000$ stars.

The completeness of our photometry was taken as the ratio of the number of recovered artificial stars over their input number in each magnitude bin. In order to account for variable crowding within the galaxy, as well as for gradients in the stellar populations (see Sections 4 and 6.1), we identified four regions within DDO 68 using isophotal contours, with Region 1 being the most central one and Region 4 the most external one. The contours that identify the four regions are overplotted on Figure 2 showing the spatial map of the resolved stars.

In Figure 4, left panels, we show the behavior of the V and I completeness as a function of magnitude for the four regions. As expected, Region 1 is the most incomplete one due to the largest crowding, with the completeness starting to drop at $V \sim 26$ and $I \sim 25$. On the other hand, the photometry is $\sim 100\%$ complete down to $V \sim 28$ and $I \sim 27$ in the most external Regions 3 and 4. The behavior of the output–input magnitudes, displayed in the right panels of Figure 4, provides a more realistic estimate of the photometric errors than σ_{DAO}. The increasing deviation of the average $m_{\mathrm{out}} - m_{\mathrm{inp}}$ toward negative values indicates the increasing effect of blending toward fainter magnitudes.

4. THE COLOR-MAGNITUDE DIAGRAM

Figure 5 shows the total m_{F814W} versus $m_{\mathrm{F606W}} - m_{\mathrm{F814W}}$ CMD of DDO 68 after applying the selection cuts described in Section 2. An estimate of the 50% completeness limit as derived from the artificial star experiments is shown in the figure, as well as the location of the TRGB as derived in Section 5. Also shown is the average size of the photometric errors in each magnitude bin. These are the errors resulting from the artificial star tests. The CMD shows a blue plume at $m_{\mathrm{F814W}} \lesssim 26.7$ and $m_{\mathrm{F606W}} - m_{\mathrm{F814W}} \simeq 0$, which is the locus of young ($\lesssim 10\,\mathrm{Myr}$) main-sequence (MS) stars and blue supergiants (BSGs; evolved stars at the hot edge of their core He-burning phase), and is typical of star-forming systems. At $m_{\mathrm{F606W}} - m_{\mathrm{F814W}} \simeq 0.9$ mag, the red plume is populated by a mix of RGB, He-burning stars near the red edge of the loop and early asymptotic giant branch (AGB) stars of intermediate mass, implying ages from $\sim 20\,\mathrm{Myr}$ up to several Gyr. At intermediate colors, the CMD samples the blue loop (BL) phase of intermediate mass stars, with ages between ~ 100 and $\sim 300\,\mathrm{Myr}$ (the oldest and faintest BL sampled by our CMD). The very red objects with $25 < m_{\mathrm{F814W}} < 26$ and $m_{\mathrm{F606W}} - m_{\mathrm{F814W}} \gtrsim 1.2$ are thermally pulsing asymptotic giant branch (TP-AGB) and Carbon stars with ages from $\sim 300\,\mathrm{Myr}$ to $\sim 2\,\mathrm{Gyr}$. More importantly, the presence of a well-populated RGB below $I \simeq 26.4$ implies a population of stars at least 1–2 Gyr old, and possibly as old as the Hubble time. The age–metallicity degeneracy affecting RGB stars normally prevents us from claiming that the redder ones are stars as old as 13 Gyr. However, the extremely low metallicity of DDO 68 makes this claim rather plausible.

In order to account for gradients in the stellar populations, we constructed separate CMDs for the four regions selected through isophotal contours (see Figure 2). The CMDs are shown in Figure 6 with superimposed the Padova PARSEC
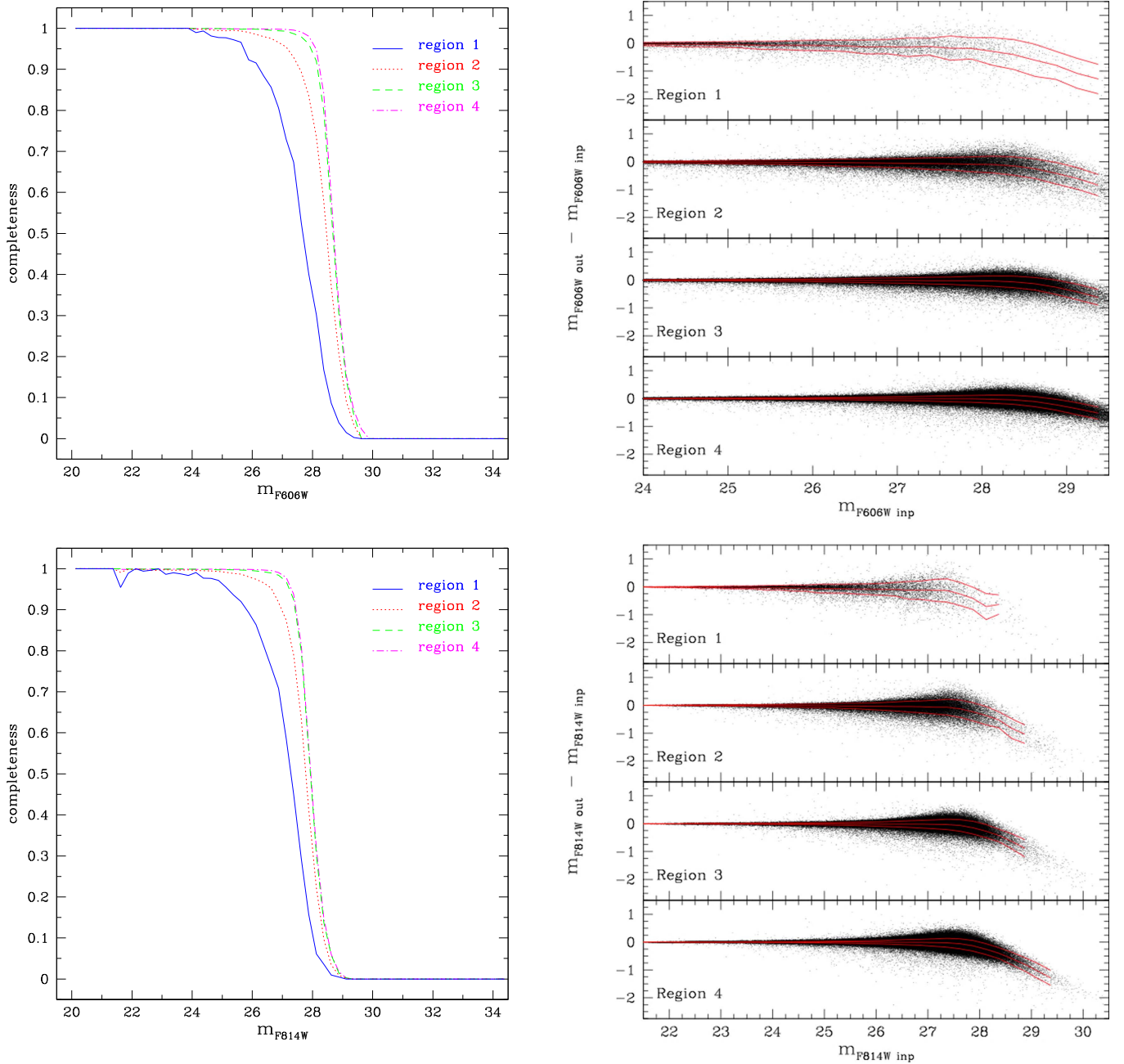
Figure 4. Completeness (left panels) and photometric errors (right panels) in *V* and *I* from the artificial star tests. The solid red curves indicate the mean of the Δmag distribution (central line) and the $\pm 1\sigma$ standard deviations.

isochrones (Bressan et al. 2012) shifted to a distance of 12.65 Mpc (Section 5) and with a foreground Galactic extinction $E(B - V) = 0.018$ (Schlegel et al. 1998); notice that in the PARSEC isochrones the thermally pulsing AGB phase is not included. These CMDs clearly show a gradient in the stellar populations, with younger stars detected predominantly in the most central regions. However, the comparison with the isochrones reveals a significant population of stars with ages of ~10 Myr or younger in Regions 2 and 3, in agreement with the presence there of a large number of H II regions (see Section 6.2). The old (>1 Gyr) RGB population is well detected everywhere but in Region 1. A more detailed analysis of the spatial distribution of the different stellar populations will be discussed in Section 6.1.

5. DISTANCE DETERMINATION

We derived the distance of DDO 68 using the magnitude of the TRGB. We show in Figure 7 the *I*-band luminosity function (LF) of stars with colors of $0.5 < V - I < 1.3$ in our catalog (the photometry was converted to the Johnson-Cousins system through the procedure outlined in Sirianni et al. (2005) in order to apply the described method).

We visually identified the TRGB as a steep increase in the LF at $I = 26.416$. There, RGB stars start to contribute to the LF, while at brighter magnitudes only red supergiants and AGB stars contribute. The dip in the LF fainter than $I \simeq 27.5$ is due to incompleteness effects. The TRGB magnitude was determined with the approach described by Cioni et al. (2000), which uses the peaks in the first and second-order derivatives
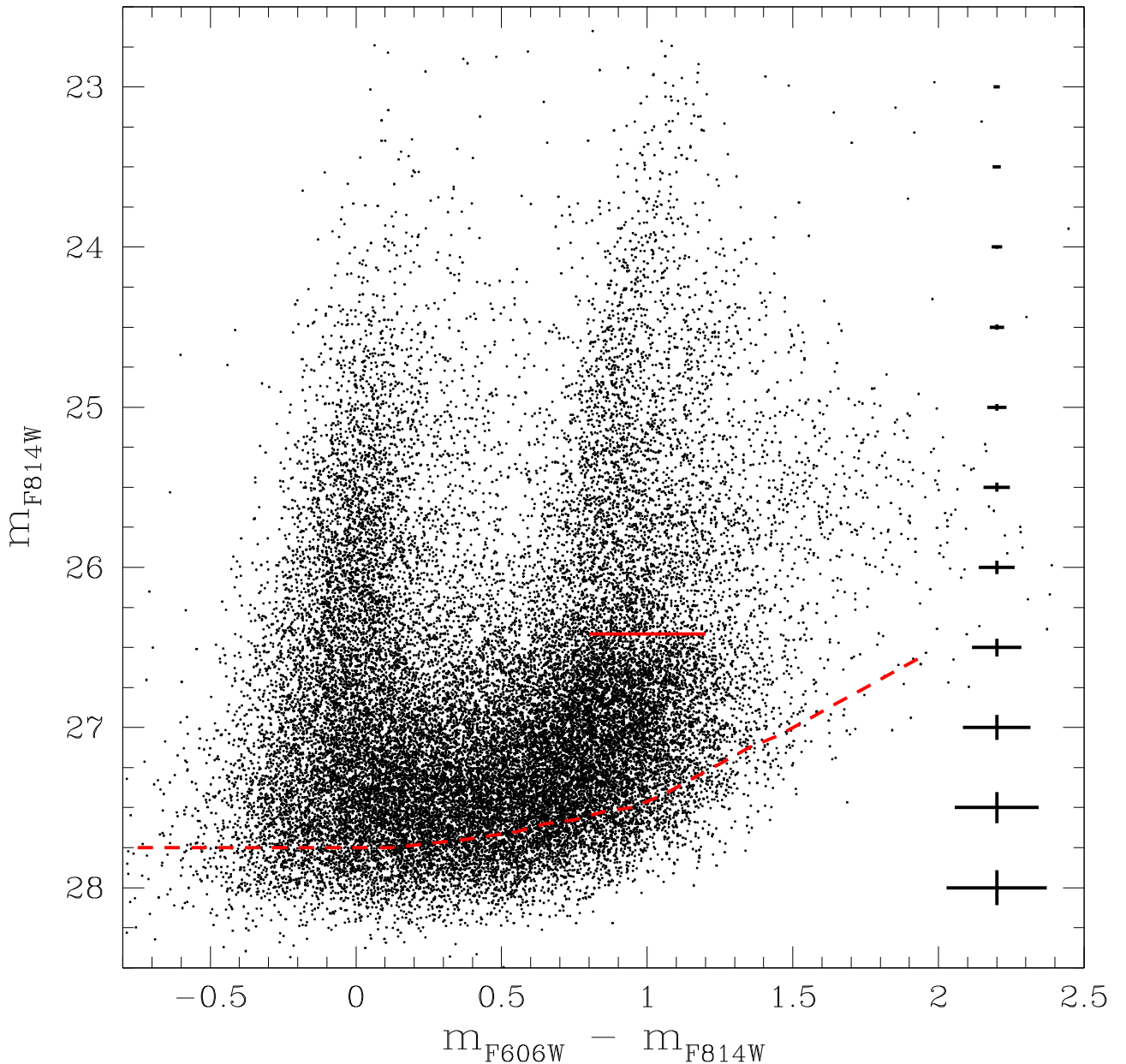
Figure 5. Total CMD of the resolved stars in DDO 68. The data are corrected for foreground extinction but not for possible extinction internal to the galaxy. The photometric errors on the right are those from the artificial star tests (1σ of the output–input distribution) assuming that the errors are uncorrelated, and that $V - I = 1$. The dashed curve provides an estimate of the 50% completeness level. The horizontal red segment indicates the magnitude of the TRGB as computed within this work.

of the LF to better identify the position of the TRGB. These peaks are shown in the middle and bottom panels of Figure 7. Once photometric errors and binning effects are accounted for, the first and second-order derivative peaks provide a TRGB magnitude of $I_{\rm TRGB,1} = 26.424$ and $I_{\rm TRGB,2} = 26.408$, respectively. The systematic error of this procedure was estimated by Cioni et al. (2000) to be $\Delta I_{\rm TRGB} = \pm 0.02$. The additional systematic errors, due to uncertainties in the photometric zero points and conversions, and in aperture corrections (Sirianni et al. 2005), is $\Delta I_{\rm TRGB} = \pm 0.023$. The random error on $\Delta I_{\rm TRGB}$ from the finite number of stars, estimated using bootstrap techniques, was found to be $\Delta I_{\rm TRGB} = \pm 0.057$. The addition of these errors in quadrature yields a total (i.e., random

plus systematic) error of ± 0.068 mag. After correcting for an I-band foreground extinction toward DDO 68 of $A_I = 0.036$ [$E(B - V) = 0.018$], we derive the final TRGB magnitude estimate of $I_{\rm TRGB,0} = 26.380 \pm 0.068$. To derive the distance modulus, we need to compare the observed TRGB magnitude with the absolute one, which was calibrated as a function of metallicity by, e.g., Bellazzini et al. (2004). At the metallicity of I Zw 18, a comparable metallicity to that of DDO 68, this is estimated at $M_{I,\rm TRGB} = -4.03 \pm 0.10$ (Aloisi et al. 2007), which implies a distance modulus of $(m - M)_0 = 30.41 \pm 0.12$ mag, i.e., $D = 12.08 \pm 0.67$ Mpc, in agreement with the value obtained by Tikhonov et al. (2014) from the same data.
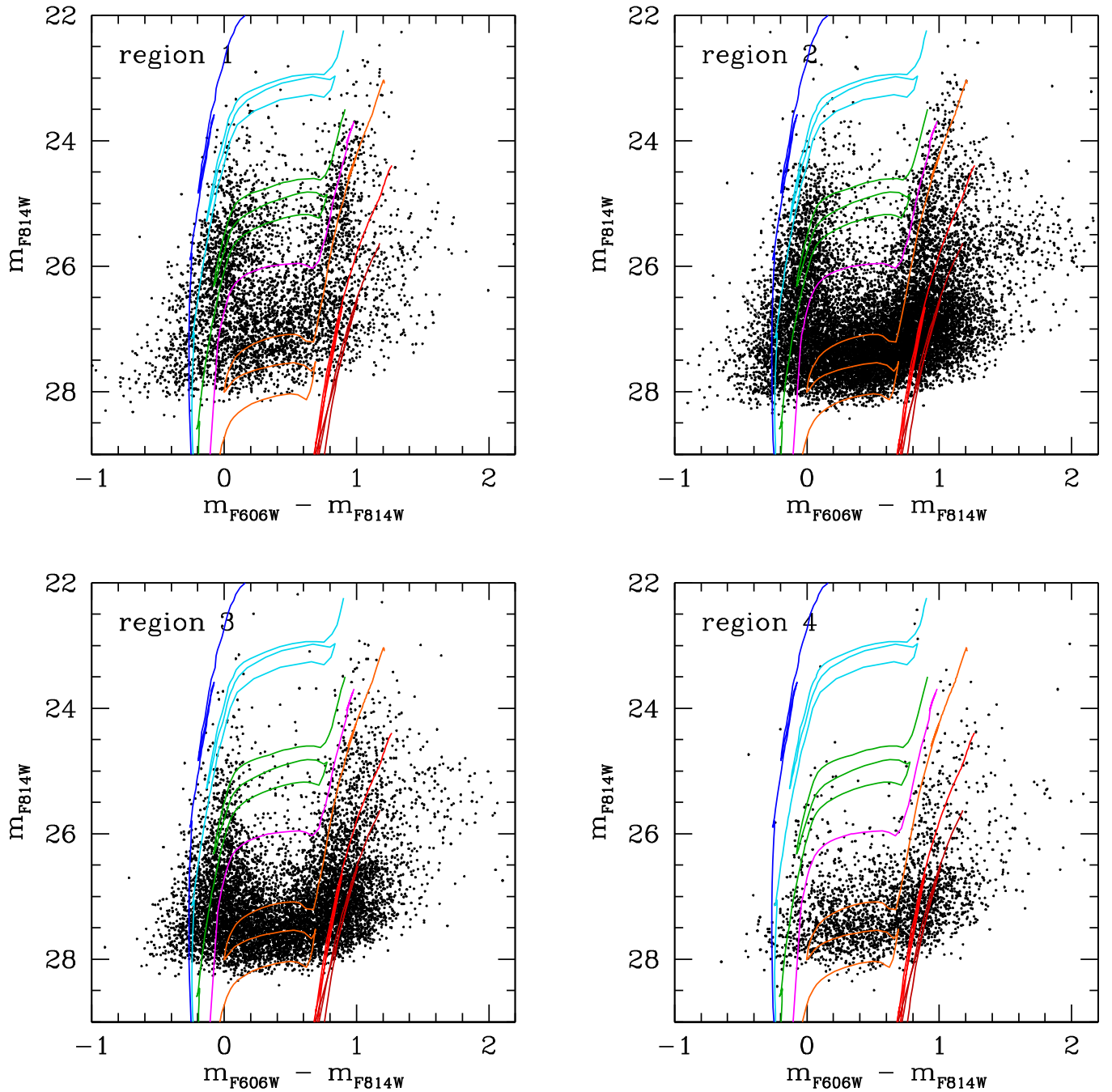
Figure 6. CMDs for the four regions of the galaxy (the region numbering goes from inside out, so Region 1 is the most internal one). The isochrones superimposed (from left to right) correspond to the following ages: 10 Myr (blue), 20 Myr (cyan), 50 Myr (green), 100 Myr (magenta), 200 Myr (orange), 2 Gyr (red), and 13 Gyr (dark red), and are plotted assuming $(m - M)_0 = 30.51$ and $E(B - V) = 0.018$.

We should, however, consider that the location of the TRGB is likely also affected by a significant blending of multiple stars in these crowded regions. The effect of blending is always to let the TRGB appear brighter. Indeed, when fitting the observed CMDs with synthetic ones to derive the SFH (see Section 7), we always found that all the evolutionary sequences are much better reproduced if the distance modulus is slightly larger, though within the uncertainties. We therefore conclude that the distance modulus of DDO 68 is $(m - M)_0 = 30.51$ and $D = 12.65$ Mpc, in agreement with the independent estimate by Cannon et al. (2014). From now on, we therefore adopt the latter distance for all applications.

6. STELLAR POPULATIONS IN DDO 68

6.1. Spacial Distribution

As a first qualitative analysis, we looked at how the different stellar populations are distributed over the galaxy. To this purpose, we used the PARSEC (Bressan et al. 2012) $Z = 0.0004$ stellar isochrones (corresponding to the metallicity of DDO 68's H II regions, Izotov & Thuan 2009) to identify a few regions corresponding to different age intervals on the CMD (see Figure 8): age < 20 Myr, $20 \lesssim$ age < 100 Myr, $100 \lesssim$ age < 300 Myr, and age > 1 Gyr (the RGB phase); we also identified the region of the carbon stars (not covered by the
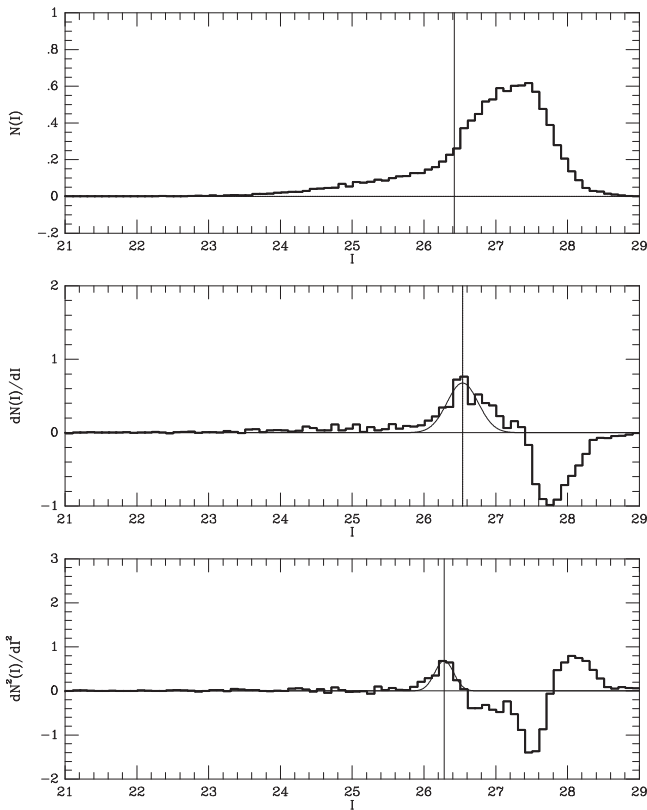
Figure 7. *I*-band LF (top) and its first (middle) and second (bottom) order derivatives for stars with $V - I$ in the range of 0.5–1.3. Magnitudes are corrected for extinction. The vertical lines indicate the position of the TRGB as derived in Section 5. The normalization of all the vertical scales is arbitrary.
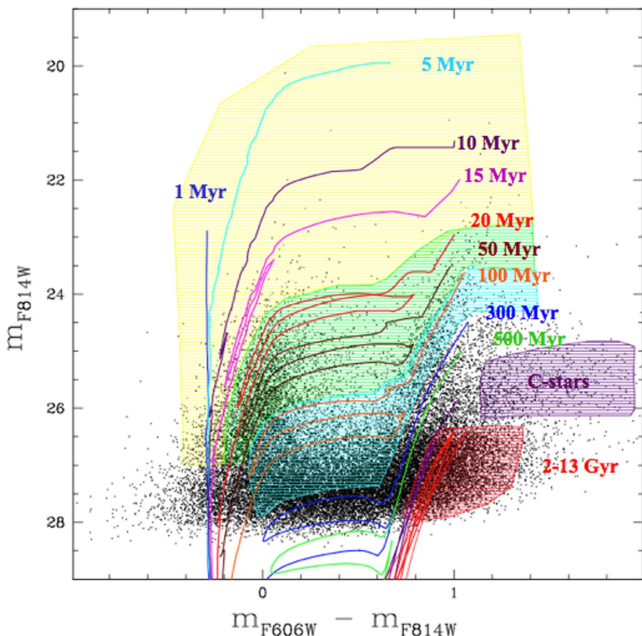

Figure 8. Selection of different age intervals identified through the $Z = 0.0004$ stellar isochrones (Bressan et al. 2012) shown and labeled in the image.

adopted isochrones), with typical ages between ∼0.3 and 2 Gyr. The spatial distribution of the stars in the different age intervals, as well as the global distribution for the total number of stars in the CMD, are shown in the star count density maps of Figure 9. For the purpose of highlighting some particular

features, the images were smoothed and arbitrarily scaled. From an inspection of the spatial maps in Figure 9, we immediately notice an important difference with the typical behavior of the stellar populations in other star-forming dwarfs, where the youngest stellar populations are preferentially concentrated toward the most central galaxy regions: in the case of DDO 68, in fact, stars younger than ∼20 Myr are also found at relatively large galactocentric distances, and in particular they appear to follow the arc-shaped structure well visible in the total spatial map. This is consistent with the presence there of numerous H II regions, as highlighted in Figure 2, which trace stars typically younger than ∼10 Myr. A similar behavior was also found in the starburst dwarf NGC 4449, for which the presence of young stars at high galactocentric distances is likely due to an accretion event (Annibali et al. 2012). As we consider increasingly older stellar populations, the distribution becomes more and more homogeneous, until the old (>1 Gyr) RGB population traces the shape of the whole galaxy really well. Notice that the paucity of RGB stars in the center of DDO 68 is an artifact due to the strong incompleteness affecting the most crowded Region 1 and does not reflect the intrinsic distribution of the old stellar populations. Interestingly, we can see the disturbed arc-shaped tail in all the age intervals, meaning that this structure is not made only of young stars as the distribution of the Hα emission might have suggested. The presence of stars of all ages in the arc-shaped structure suggests that this is a possible dwarf galaxy interacting with the central body of DDO 68, since stars older than ∼1 Gyr would not be able to remain in the form of a gravitationally unstable arc. Indeed, in a recent work, Tikhonov et al. (2014) suggested that DDO 68 consists of two distinct objects: a more massive central galaxy, DDO 68 A, traced by the spatial distribution of the bulk of the old stars, and a dwarf galaxy in interaction with DDO 68 A, namely DDO 68 B, corresponding to the arc-shaped structure, a hypothesis that we find very interesting and worthy of further investigation.

In the RGB spatial map, we also recognize a small concentration of stars toward the upper right edge of the ACS chip, noticed also by Tikhonov et al. (2014); new results on this feature are presented in a separate paper based on new Large Binocular Telescope (LBT) data with a much larger field of view (Annibali et al. 2016).

6.2. H II Regions

The F658N narrow band filter allows us to study how the Hα emission is located within the galaxy and to identify the very recent concentrations of SF. In fact, the Hα recombination line is one of the most widely used tracers of recent SF, since it comes from the recombination of gas ionized by photons of massive stars ($>20\,M_\odot$) and thus is expected to be observed over the typical lifetimes of massive stars (<10 Myr) (Leitherer et al. 1999). Thus, the ionized gas emission traces the youngest SF and provides an important piece of information on the SFH and on the dynamical interactions of the galaxy. A quite interesting and uncommon feature is that the H II regions in DDO 68 are placed mostly in the outer parts (see Figures 1 and 2) suggesting some external effect to trigger the SF. As already discussed, this could be the presence of another object that has recently interacted with DDO 68. We selected 8 H II regions based on the gas distribution, and visually analyzed the CMDs of their resolved stars (Figure 10) finding that they are predominantly populated by young blue-plume stars. A
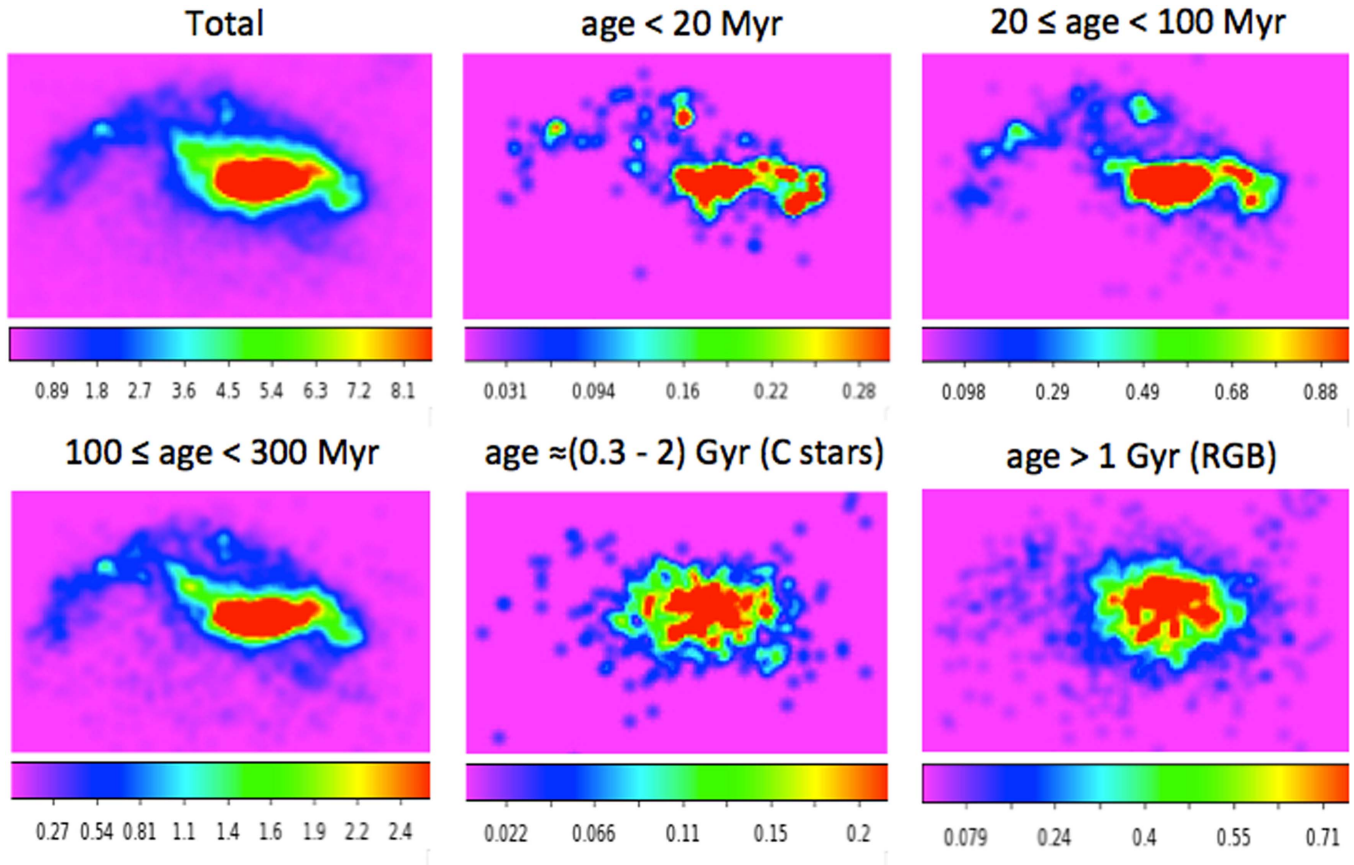
Figure 9. Density maps of stars observed in different evolutionary phases within DDO 68, as selected through their position in the CMD (see Figure 8). The scale is in units of stars/arcsec^2.

comparison with stellar isochrones indicates that stars younger than ~10–20 Myr are found in these regions, in agreement with the presence of ionized gas. The regions in Figure 10 were labeled following Pustilnik et al. (2005) and Izotov & Thuan (2009).

7. STAR FORMATION HISTORY

The SFH of DDO 68 was derived by comparing the observed CMDs with synthetic ones, following the method originally devised by Tosi et al. (1991). The synthetic CMDs were constructed as linear combinations of "basis functions" (BFs), i.e., contiguous star formation episodes whose combination spans the whole Hubble time. Observed and synthetic CMDs were compared through a statistical analysis; to this purpose, we adopted two independent procedures: one originally developed by R. P. van der Marel and described in Grocholski et al. (2012), based on the code SFHMATRIX, and the other devised by M. Cignoni and described in Cignoni et al. (2015), based on SFERA (Star Formation Evolution Recovery Algorithm).

We consider it useful to compare the SFHs derived with the two different approaches to estimate which results are robust and which are more uncertain or even artifacts of the chosen minimization algorithms.

7.1. Basis Functions

The construction of the BFs is based on the combination between stellar evolution models and observational uncertainties (e.g., photometric errors, incompleteness) of the examined

galaxy region. We created the BFs starting from the latest (V.1.2S) Padova PARSEC isochrones (Bressan et al. 2012), which include the pre-main-sequence evolutionary phase (while the TP-AGB phase is still not included). We adopted a Kroupa IMF (Kroupa 2001) from 0.08 to 120 $M_\odot$ and we assumed a 30% fraction of binary stars, whose masses were extracted from the same IMF of the "main" population.

The BFs were computed up to an age of ~13.5 Gyr with a logarithmic time duration of $\Delta \log(\mathrm{age}) = 0.25$, except for ages younger than 1 Myr, which were grouped into a single time bin. The logarithmic step is chosen to take into account the lower time resolution as a function of the look-back time. The star formation rate (SFR) is assumed to be constant within each episode.

The "theoretical" BFs were convolved with the characteristics of the data, i.e., distance, foreground and internal extinction, as well as the completeness and photometric errors derived from the artificial star tests. Absolute magnitudes were converted into apparent ones applying a foreground reddening of $E(B - V) = 0.018$ from the NASA/IPAC Extragalactic Database[11], and a distance modulus allowed to vary by 1 mag around the value $(m - M)_0 = 30.41$ mag derived from the TRGB (see Section 5). Eventually, the best value to fit all the evolutionary sequences and LFs turned out to be $(m - M)_0 = 30.51$.

---

[11] The NASA/IPAC Extragalactic Database is operated by the Jet Propulsion Laboratory, California Institute of Technology, under contract with the National Aeronautics and Space Administration. See https://ned.ipac.caltech.edu.
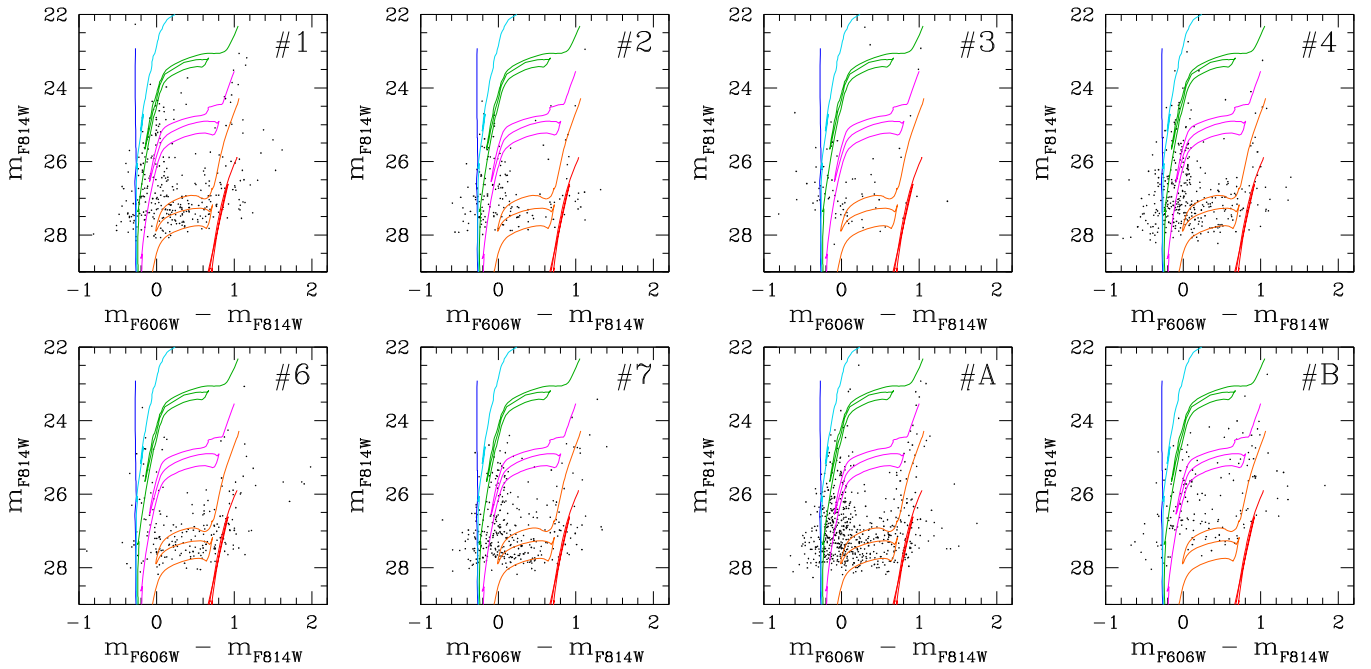
Figure 10. CMDs of the H II regions in DDO 68. The isochrones superimposed (from left to right) correspond to the following ages: 1 Myr (blue), 10 Myr (cyan), 20 Myr (green), 50 Myr (magenta), 200 Myr (orange), and 2 Gyr (red). The numbers follow the labeling by Pustilnik et al. (2005) and Izotov & Thuan (2009) except for the last two regions (A and B), which they do not take into account in their analysis.

To incorporate observational effects and systematic errors (due to, e.g., photometric blends), we assigned photometric errors to the synthetic stars using the difference between output and input magnitudes of the artificial stars (see Figure 4). To make sure that all the stellar evolutionary phases are well populated in spite of the incompleteness, the synthetic CMDs are generated with a very large number of stars. The comparison with the observational CMD is, however, performed considering the number of stars actually present in the latter. The comparison is done on the Hess diagram, i.e., considering the density of points in the CMD. To this purpose, the BFs, as well as the observed CMD, are pixelated into a grid of n color-bins and m magnitude-bins.

We have used the two different procedures SFERA and SFHMATRIX to identify the weighted combination of BFs that best reproduces the observational CMDs and thus the best SFH. In the following, we describe the two statistical codes used for the derivation of the SFH.

7.2. The SFERA Procedure

To explore the wide parameter space involved in the derivation of the SFHs, SFERA combines a genetic algorithm with a local search routine, as described in detail by Cignoni et al. (2015).

The metallicity is treated as a free parameter. We do not assume an age–metallicity relation nor the same metallicity for all the stars; however, since we have the information on the current metallicity (corresponding to $Z \sim 0.0004$) from the H II regions, we allow the metallicity to vary in the range [0.0002–0.002]. For all regions, the metallicity inferred by SFERA in the youngest bins is between $Z \sim 0.00035$ and $Z \sim 0.0005$, consistent with the observed values from the H II regions.

We end up with a library of $j \times k$ 2D histograms, $BF_{m,n}(j, k)$, that can be linearly combined to express any observed CMD, as in Equation (1). The coefficients $w(j, k)$ are the weights of each of the $BF_{m,n}(j, k)$, and represent the SFR at the time step j and metallicity step k. The sum over j and k of $w(j, k) \times BF_{m,n}(j, k)$ gives the total star counts $N_{m,n}$ in the CMD bin (m, n):

$$N_{n,m} = \sum_j \sum_k w(j, k) \times BF_{m,n}(j, k). \tag{1}$$

The minimization of the residuals between data and models is implemented in SFERA taking into account the low number counts in some CMD cells, so we follow a Poissonian statistics, looking for the combination of BFs that minimizes a likelihood distance between model and data. This corresponds to the most likely SFH for these data, with an uncertainty given by the sum in quadrature of a statistical error (computed through a data bootstrap) and a systematic error (obtained by re-deriving the SFH with different age and CMD binnings, even if this tends to smooth out the SFH). The Poisson based likelihood function we chose is

$$\chi_P = \sum_{i=1}^{N\text{bin}} \text{obs}_i \ln \frac{\text{obs}_i}{\text{mod}_i} - \text{obs}_i + \text{mod}_i \tag{2}$$

where mod_i and obs_i are the model and the data histogram in the i-bin. This likelihood is minimized with a hybrid-genetic algorithm, which combines a classical genetic algorithm (Pikaia[12]) with a local search (Simulated Annealing). This allows us to take advantage of the exploration ability of the former, which scans the parameters space in more points

---

[12] Routine developed at the High Altitude Observatory and available in the public domain: http://www.hao.ucar.edu/modeling/pikaia.php.

simultaneously and thus is not too sensitive to the initial conditions, and the capability of the latter of local exploration of the space and faster convergence. The proposed algorithm alternates two phases: the search for a quasi-global solution by the genetic algorithm and the local search by the other one, which increases the solution accuracy.

7.3. The SFHMATRIX Procedure

The SFHMATRIX code solves a non-negative least-squares matrix problem to identify the SFH that best reproduces the Hess diagram of the observational CMD in a χ^2 sense. The minimization problem is addressed as the solution of a matrix equation:

$$\sum_j w(j) \times \mathrm{BF}_{m,n}(j) = \rho_{m,n} \pm \Delta\rho_{m,n} \qquad (3)$$

where $\rho_{m,n}$ is the star density in the observed CMD, $\Delta\rho_{m,n}$ is the corresponding Poisson uncertainty, and m and n are the Hess diagram pixels; the density $\rho_{m,n}$ is given by the integer number of stars $L_{m,n} \geqslant 0$, which is detected in the Hess diagram pixel (m, n), divided by the area of that pixel. The adopted Poisson error on the detected number of stars is $\max(1, \sqrt{L_{m,n}})$, hence

$$\frac{\Delta\rho_{m,n}}{\rho_{m,n}} = \frac{\max(1, \sqrt{L_{m,n}})}{L_{m,n}}. \qquad (4)$$

$\mathrm{BF}_{m,n}(j)$ is the density of stars in the BF corresponding to the jth time step in the same pixel of the Hess diagram, weighted for the coefficient $w(j)$ (see Grocholski et al. 2012 for the details). Since SFHMATRIX is primarily used as a cross-check and validation of the SFERA results, we use BFs of fixed low metallicity ($Z \sim 0.0004$).

The errors on the SFH are estimated by drawing many Monte Carlo realizations from the best-fit SFH and analyzing them with the same procedure used for the real data.

Mighell (1999) demonstrated that a χ^2 minimization is generally biased when data are Poisson distributed; in particular, assuming the uncertainty on the data $\Delta\rho_{m,n} = \max(1, \sqrt{L_{m,n}})$ leads to an underestimation of the true mean of the Poisson distribution. Given this uncertainty, we use the χ^2 approach only as a comparison of the SFERA results. In the next sections, we explore and compare the results from the two different adopted procedures in detail and we will come back to this bias in Section 7.7.

7.4. Region 1

Panel (a) of Figure 11 shows the observed CMD of the most crowded Region 1 of DDO 68, together with the synthetic realizations inferred from the best-fit solutions of the SFERA (panel (b)) and SFHMATRIX (panel (c)) codes. We excluded from the minimization the cells of the CMD with a completeness below 30% where the uncertainties become significant. We used a lower completeness threshold with respect to the other regions in order to reach at least the TRGB and have a strong constraint on the CMD. We run several tests using a different completeness limit (up to 50%) and this yielded results that are qualitatively similar. We choose to keep the results with a completeness down to 30% to include the
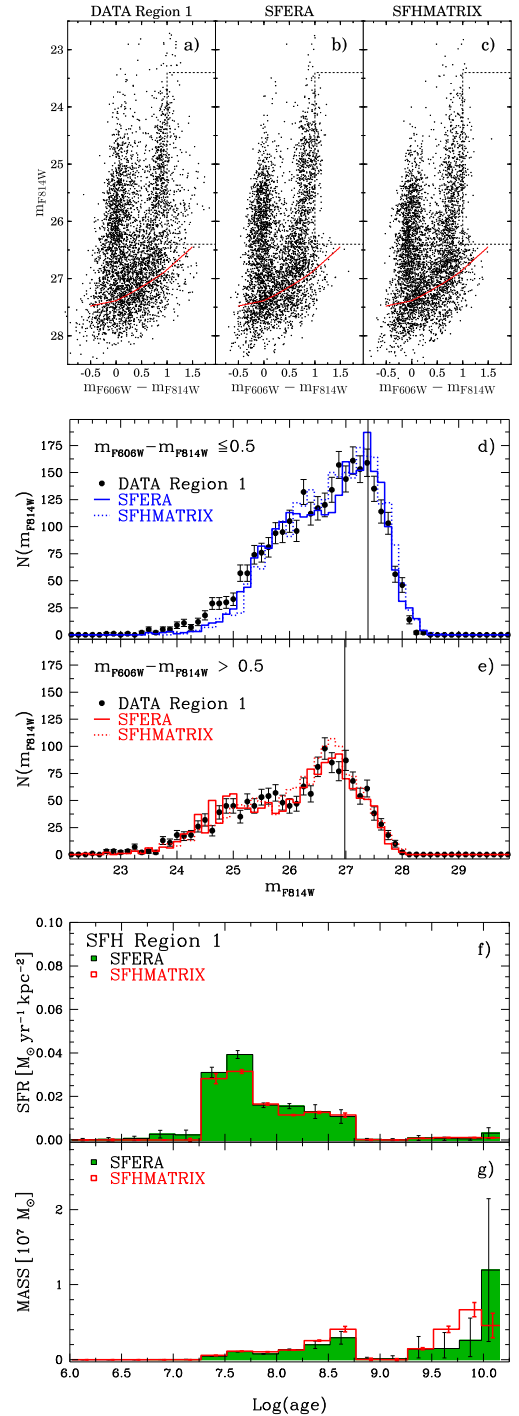

Figure 11. Results of the synthetic CMD method for Region 1. Top panels: (a) observed CMD for Region 1, (b) best-fit synthetic CMD with SFERA, and (c) best-fit synthetic CMD with SFHMATRIX (both obtained considering only the region with completeness above 30% indicated by the red solid curve). The dotted box shows the TP-AGB region that was excluded from the minimization. Middle panels: LF in blue (d) and red (e) for the observed (black points with Poissonian error) and synthetic CMDs (solid line for SFERA, dotted line for SFHMATRIX). The vertical lines indicate the average faintest magnitudes that were considered for the fit. Bottom panels: best-fit SFH (f) normalized over the area of the region and recovered stellar mass (g) with SFERA (green solid histograms) and SFHMATRIX (red histograms). Notice that the error bars coming out from SFHMATRIX have to be considered as lower limits to the real uncertainties of the solution, since only statistical errors are included and the metallicity is fixed.

RGB stars, since they are the only signature of epochs older than 1–2 Gyr ago; we do take into account the larger uncertainty due to this choice and we are confident that this does not affect the main conclusions of the paper.

When using SFHMATRIX, we created a grid with a constant cell size of 0.5 both in color and in magnitude: given the low number of stars in Region 1, this cell size allows us to minimize the statistical fluctuations without loosing information on the CMD. For the same reason, we treated the box at $0.5 < m_{F606W}-m_{F814W} < 1.3$ and $26.4 < m_{F814W} < 29$ (i.e., the RGB) as a single pixel, while we excluded from the minimization the box at $1 < m_{F606W}-m_{F814W} < 2$ and $23.4 < m_{F814W} < 26.4$, corresponding to the TP-AGB phase, which is not included in the PARSEC isochrones yet.

In SFERA, where flexibility in the construction of the grid is possible, we chose a quite large cell size (0.5 both in color and magnitude) for the brightest stars with $m_{F814W} < 24$ to balance the low statistics caused by the low number of bright stars; we chose an intermediate cell size (0.1 in color, 0.2 in magnitude) for the blue and red plumes and for the lower MS; for the RGB, instead we implemented a variable random binning from 1 to 16 cells in the box $0.5 < m_{F606W}-m_{F814W} < 1.3$ and $26.4 < m_{F814W} < 29$, which we changed at every bootstrap in order to minimize the bin dependence of the results.

To reproduce the observed CMD and LF in Region 1, as well as in all the other regions of DDO 68, we found it more satisfactory to adopt a slightly higher distance modulus than that derived from the TRGB (that is $(m - M)_0 = 30.51$ instead of $(m - M)_0 = 30.41$); this larger distance modulus, which is still inside the errors of the previous determination, implies a distance of 12.65 Mpc.

We show in Figure 11 the solutions found by the two codes for the best CMD (b–c), LF (d–e), and SFH (f–g). It is evident that the codes are both able to well reproduce the overall morphology of the observed CMD, though with some differences. In particular, both codes tend to underpredict the number of stars in the blue LF ($m_{F606W}-m_{F814W} \lesssim 0.5$) at $24 < m_{F814W} < 25.25$, i.e., the BSGs. A similar problem was found for another very-low-metallicity dwarf galaxy, I Zw 18, for which we derived the SFH (Annibali et al. 2013). As already discussed in that study, possible explanations for the observed discrepancy are: (1) the completeness behavior with magnitude is not properly taken into account, because of the severe crowding of this central region; (2) some of the most luminous blue stars in the CMD are not actually single objects but blends of two or more blue stars; and (3) the timescales for the evolution of massive stars in the brightest post-MS phase are not properly modeled.

It is plausible that models including additional parameters, like stellar rotation (Meynet & Maeder 2002), could improve the fit of the brightest objects in the CMD, but these models are not implemented yet for DDO 68's metallicity.

Panels (f) and (g) of Figure 11 shows the best-fit SFHs (normalized over the area of the region) and the stellar mass assembled in the different time bins, where the solid green and the red histograms are the output of SFERA and SFHMATRIX, respectively. These SFHs are quite in agreement with each other, and clearly show an old activity, once again confirming the presence of a population of stars at least 1 Gyr old and probably as old as the Hubble time. Notice that the low uncertainty inferred for some bins with very low SF (e.g.,

8.75–9.25) could be an artifact of the bootstrap approach (see Dolphin 2013 for a detailed discussion). The mass in stars at epochs older than 1 Gyr is ~70% of the total stellar mass formed in this region. There is no evidence of a very young (<5 Myr) SF episode, while the strongest burst ($SFR_{peak} \simeq 3.9 \times 10^{-2}$ $M_\odot$ yr^{-1} kpc^{-2}) occurred between 20 and 60 Myr ago.

The results for the average SFR and for the stellar mass formed in different time intervals are summarized in Table 1.

7.5. Region 2

Figure 12 shows the results for Region 2. We excluded from the fit the region of the CMD where the completeness is below 50%. Given the larger number of stars with respect to Region 1, we chose to use a pixel size of only 0.25 in both color and magnitude when running SFHMATRIX. We masked again the region of the TP-AGB phase. For SFERA, we kept the same (variable) binning as for Region 1.

The blue LF in panel (d) of Figure 12 shows that SFHMATRIX underpredicts the counts at $27 < m_{F814W} < 27.5$, while SFERA does so between 27 and 27.25, and both codes slightly overpredict the counts below 27.5; these regions correspond to the lower part of the MS where probably both the spatial resolution and the completeness of the photometry are degrading fast. For what concerns the red LFs ($m_{F606W}-m_{F814W} > 0.5$), SFERA provides a quite good agreement in the brightest bins, and at $\sim\pm0.5$ magnitudes around the TRGB; on the other hand, we notice an underprediction of counts at $25 < m_{F814W} < 26$, where the (not-simulated) TP-AGB stars are located, and at $27 < m_{F814W} < 27.5$. The SFHMATRIX code, instead, provides a better agreement in this magnitude range, but tends to overpredict the counts around the TRGB.

The SFH shows an overall trend very similar to that of Region 1, but the SFRs are almost 10 times lower ($SFR_{peak} \simeq 0.6 \times 10^{-2} M_\odot$ yr^{-1} kpc^{-2} between 20 and 60 Myr) and were in fact multiplied by a factor of 10 in the plot to make them more visible. Also in this region, we find the majority of the mass locked in the oldest (>1 Gyr) stars, while there is no evidence for significant recent activity.

This is the region where we find the largest differences between the results from the two codes, particularly in the formed stellar mass. In general, we consider SFERA more reliable because it minimizes an actual likelihood using Poissonian statistics, and does not make the simplifying assumption of Gaussian statistics that is inherent to the χ^2 minimization of SFHMATRIX. However, for the main characteristics of DDO 68 implied by our SFHs, the codes yield broadly consistent results (see Table 1).

7.6. Region 3

For Regions 3 and 4 of DDO 68, we kept the same binning of Region 2 and the same completeness limit of 50%. As shown in Figure 13, this is the best reproduced region, both in the CMD and in the LFs. With SFERA there are no relevant discrepancies between the data and the models, while with SFHMATRIX there is an underprediction of the blue counts at $m_{F814W} \sim 27.5$ and an overprediction of the red counts at $26.5 < m_{F814W} < 27$.

Table 1
Summary of the Results for SFRs and Stellar Mass in the Four Regions

| Region | Area (kpc^2) | $\langle SFR \rangle_{age<1\,Gyr}$ ($M_\odot$ yr^{-1} kpc^{-2}) | | $M_{\star TOT}$ ($10^7\,M_\odot$) | | $M_{\star age>1\,Gyr}$ ($10^7\,M_\odot$) | |
		SFERA	SFHMATRIX	SFERA	SFHMATRIX	SFERA	SFHMATRIX
1	1.1	$(7.91 \pm 0.91) \times 10^{-3}$	$(9.68 \pm 0.37) \times 10^{-3}$	2.62 ± 1.04	2.74 ± 0.20	1.75 ± 1.03	1.67 ± 0.19
2	9.2	$(1.28 \pm 0.12) \times 10^{-3}$	$(1.98 \pm 0.03) \times 10^{-3}$	6.94 ± 2.49	7.85 ± 0.19	5.76 ± 2.49	6.03 ± 0.19
3	26.5	$(2.17 \pm 0.20) \times 10^{-4}$	$(3.66 \pm 0.07) \times 10^{-4}$	2.41 ± 0.84	2.61 ± 0.10	1.83 ± 0.84	1.64 ± 0.10
4	68.5	$(0.31 \pm 0.05) \times 10^{-4}$	$(0.37 \pm 0.02) \times 10^{-4}$	0.93 ± 0.34	0.94 ± 0.07	0.72 ± 0.34	0.68 ± 0.07

The SFRs per unit area plotted in panel (f) are multiplied by a factor of 10^2 to make them more visible; this is the region where very recent SF activity is found by both codes. This is in agreement with the fact that the majority of the nebular emission is found in this region. The remaining evolution of the SF is quite similar to the other regions, but with lower rates (SFR$_{peak}$ $\simeq 7.5 \times 10^{-4}\,M_\odot$ yr^{-1} kpc^{-2} between 20 and 60 Myr).

7.7. Region 4

Figure 14 shows the CMD, LFs, and SFH of the most external region of the galaxy. There are very few stars here and a strong contamination from background galaxies. In fact, as expected, SFHMATRIX has some trouble reproducing the right number of stars as can be noticed from the LFs. In both the blue and red LFs SFHMATRIX underpredicts the counts, also in the RGB region. SFERA instead reproduces well the blue LF, while it underpredicts the number of stars in the red LF at $27 < m_{F814W} < 27.5$. The plotted SFRs, in this case, are multiplied by a factor of 10^3, and are very low in general, showing a peak two bins older than the previous regions (SFR$_{peak}$ $\simeq 0.8 \times 10^{-4}$ $M_\odot$ yr^{-1} kpc^{-2} between 100 and 200 Myr). This is not surprising since we expect this region to host mainly old populations of stars as discussed in Section 6.1. The oldest bins provide again the most relevant contribution to the formed stellar mass.

The total average SFR over the whole galaxy is $\simeq 0.01\,M_\odot$/ yr, and the corresponding astrated mass over the Hubble time is $M_{\star TOT} \simeq 1.3 \times 10^8\,M_\odot$.

Overall, the general good agreement between the solutions of SFHMATRIX and SFERA seems to suggest that the χ^2 bias is not significantly affecting the results.

7.8. DDO 68 B

The peak in the star formation activity between $\sim$30 and $\sim$50 Myr that we find in all regions of DDO 68 hints that this epoch may have been affected by a merging/accretion event between two different bodies, as suggested by Tikhonov et al. (2014). For this reason, we performed a separate analysis of the arc-shaped structure (dubbed by Tikhonov et al. 2014 DDO 68 B) to explore also the possibility that the increased young star formation in Region 3 could be the result of this interaction.

In Figure 15, we show two selections of stars falling in the tail for which we rederived the SFH. The results are shown in Figure 16 (the SFRs per unit area are multiplied by a factor of 10^2 as for Region 3). The SFH of the candidate accreted satellite in the last hundreds Myr is qualitatively similar to that of Region 2, which can be considered as representative of the main body, though the SF activity in configuration 2 of the tail

is definitely more skewed toward more recent epochs, and close to absent at epochs older that 1 Gyr, as if the activity in the candidate satellite was mostly triggered when the interaction with the main body became strong. The young peak is the same as in Region 3, as expected since most of the Hα emission is in common. However, the SFR normalized over the area in each bin is roughly double in the tail with respect to the whole Region 3, since it has a smaller area but the majority of the young and intermediate stars.

The average SFR over the last $\sim$1 Gyr in the tail configuration 1 is $\langle SFR \rangle_{Tail\,1} \simeq 3 \times 10^{-4}\,M_\odot$ yr^{-1} kpc^{-2} while the total formed stellar mass is $M_{\star\,Tail\,1} \simeq 1.2 \times 10^7\,M_\odot$ that is $\sim$1/10 of the stellar mass of the whole galaxy. In configuration 2, they are $\langle SFR \rangle_{Tail\,2} \simeq 4 \times 10^{-4}\,M_\odot$ yr^{-1} kpc^{-2} and $M_{\star\,Tail\,2} \simeq 0.6 \times 10^7\,M_\odot$ respectively. The metallicity in the most recent bin of configuration 2 is $Z \sim 0.0008$, so slightly higher than that of the other regions; however, the uncertainties on this determination prevent a firm conclusion.

The presence of recent SF in Region 3 is thus compatible with the merging/accretion scenario, explored in more detail by Annibali et al. (2016).

8. DISCUSSION AND CONCLUSIONS

In this paper, we presented several results on the star-forming dwarf DDO 68, i.e., an accurate distance determination, a qualitative analysis of the spatial distribution of the different stellar populations, a detailed SFH based on the synthetic CMD method, and some very preliminary dynamical considerations. Here we summarize and discuss the main results obtained.

From the TRGB method, we derived a distance modulus of $(m - M)_0 = 30.41 \pm 0.12$ mag, i.e., a distance of $D = 12.08 \pm 0.67$ Mpc. However, during our synthetic CMD analysis, we found that it was more satisfactory to use a slightly higher distance modulus, i.e., $(m - M)_0 = 30.51$, implying a distance of $D = 12.65$ Mpc, still inside the errors of our TRGB determination, and closer to the distance of $D = 12.74 \pm 0.27$ Mpc adopted by Cannon et al. (2014). From the presence of a well-populated RGB, we concluded that DDO 68 hosts a population of stars at least 1–2 Gyr old (and possibly as old as a Hubble time), allowing us to reject the hypothesis that this is a young system experiencing its first burst of SF at recent epochs. The same conclusion was reached for the BCD I Zw 18, with a similarly low metallicity, for which we clearly detected the RGB (Aloisi et al. 2007), and were able to provide a lower limit for the stellar mass formed at epochs older than 1–2 Gyr ago (Annibali et al. 2013). Another galaxy worth mentioning in this context is Leo P, a recently discovered star-forming dwarf galaxy that has the same extremely low metallicity of DDO 68 and I Zw 18. Leo P is
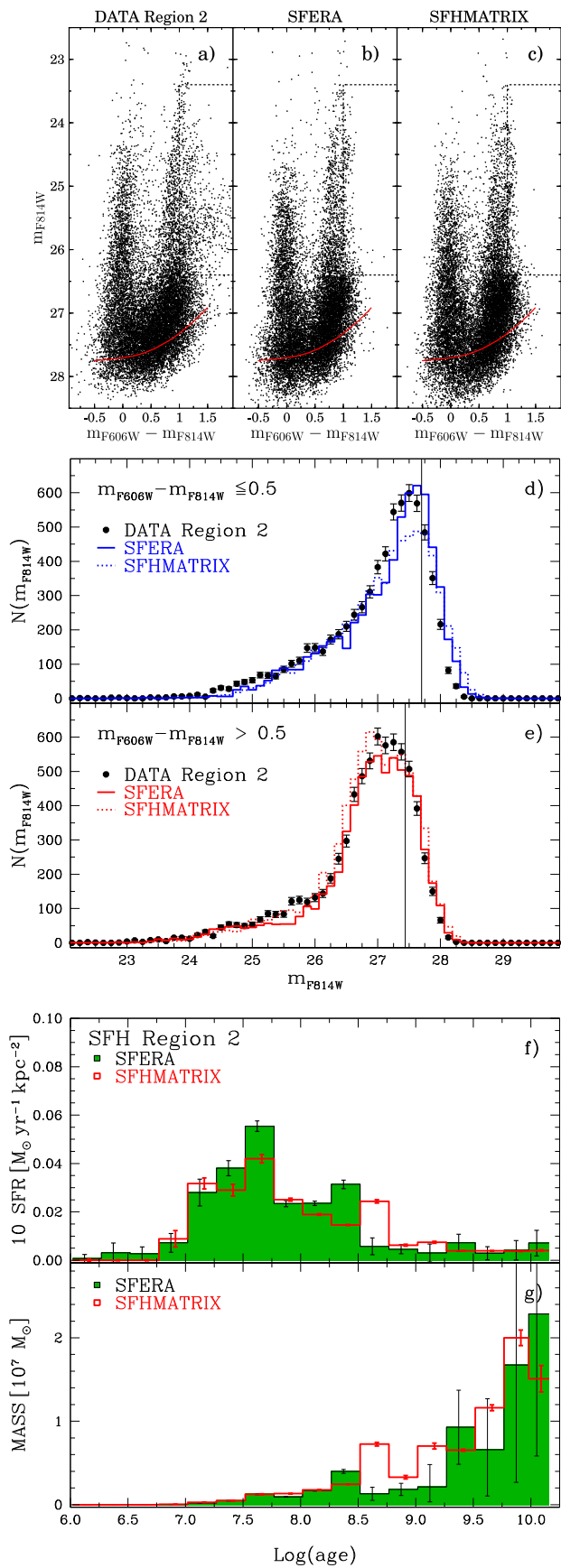
Figure 12. Same as Figure 11 but for Region 2 (the best fit is performed in the region with completeness above 50%). Notice that in this case the SFRs of panel (f) are multiplied by 10.
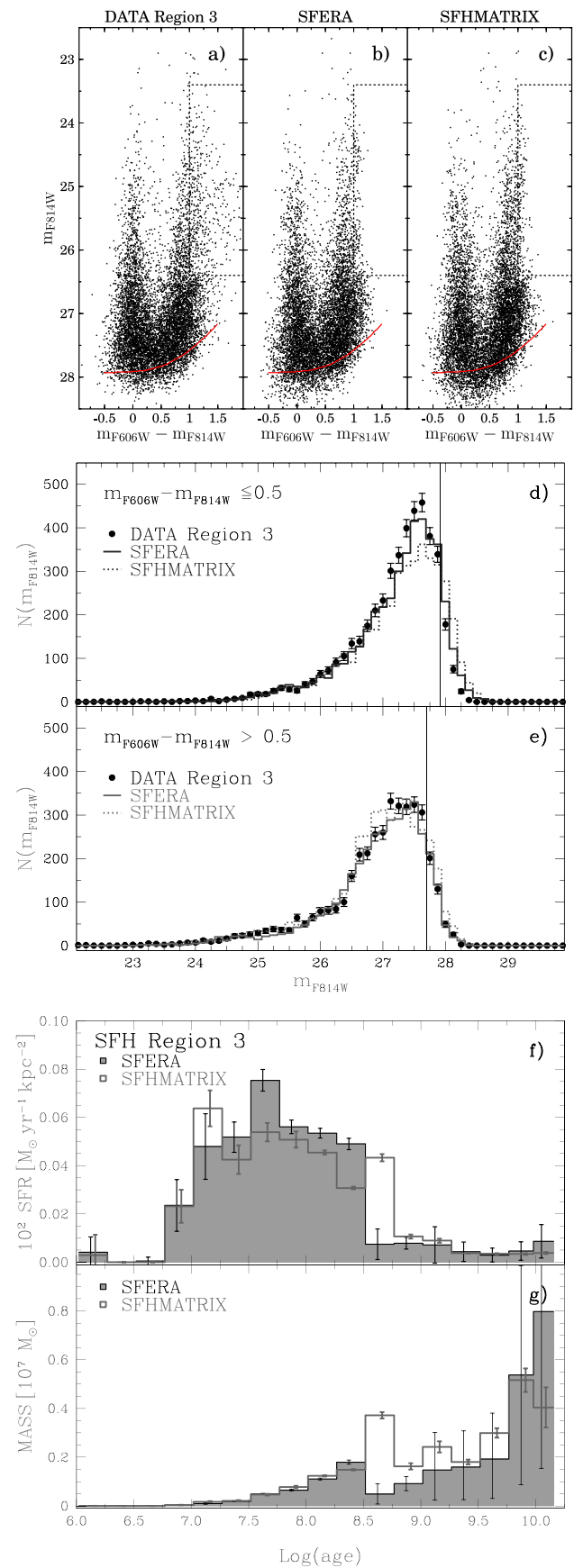
Figure 13. Same as Figures 11 and 12 but for Region 3. Notice that in this case the SFRs of panel (f) are multiplied by 100.
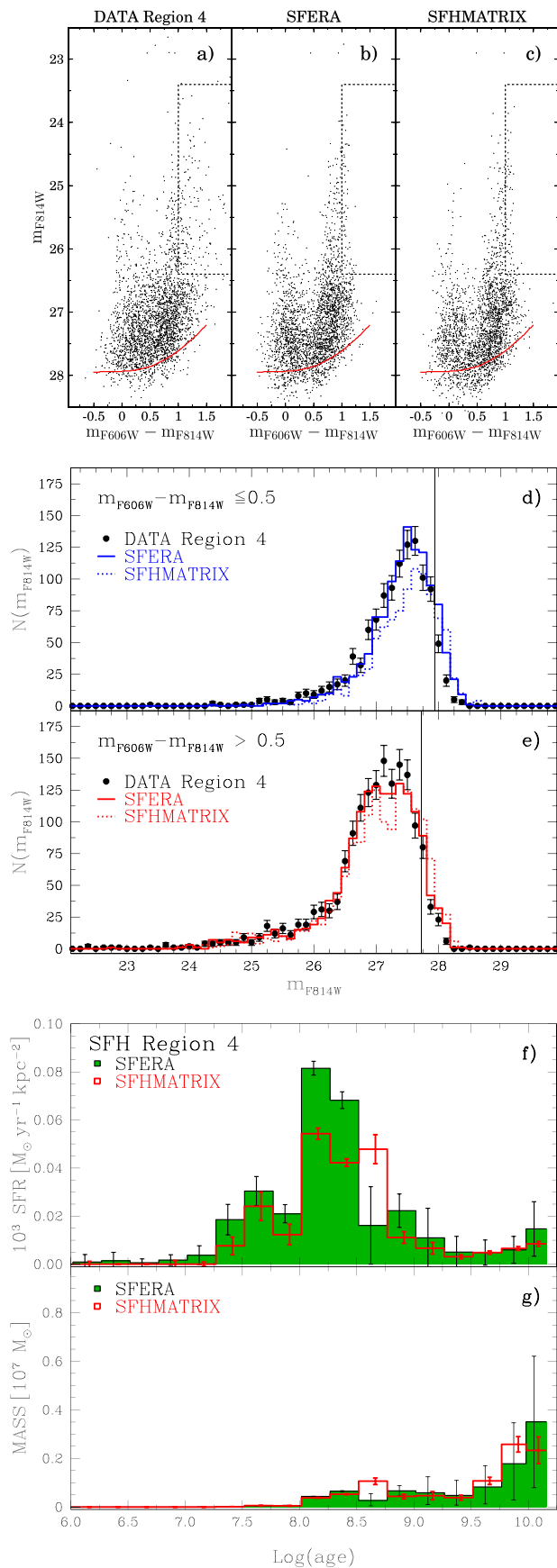
Figure 14. Same as Figures 11–13 but for Region 4. Notice that in this case the SFRs of panel (f) are multiplied by 1000.
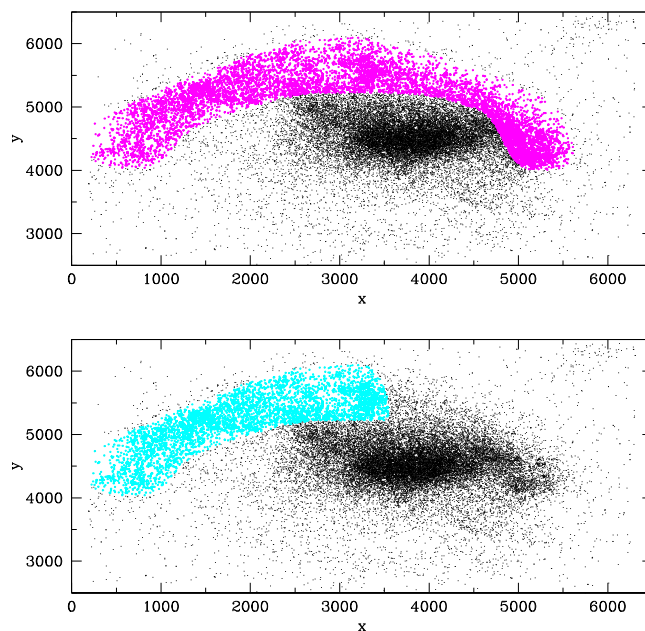

Figure 15. Map of the stars in DDO 68 with enhanced in magenta and cyan two possible configurations of the arc-shaped structure identified as DDO 68 B and used for a separate derivation of the SFH.
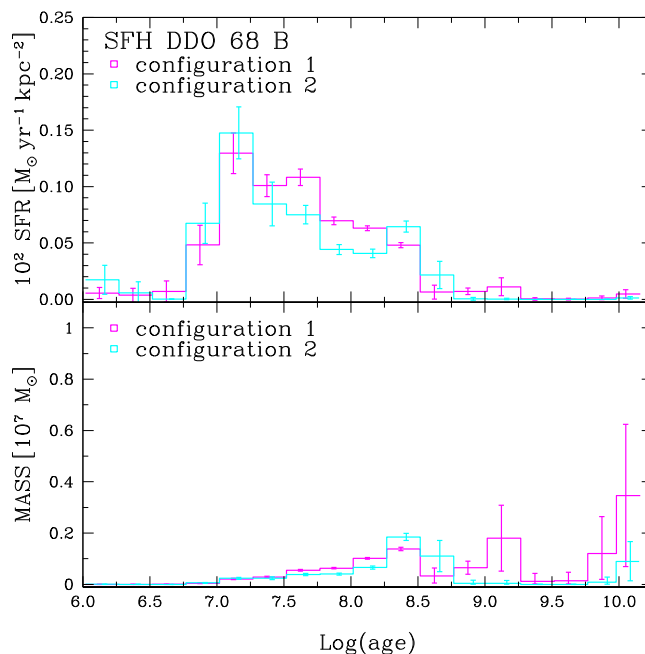

Figure 16. SFHs for stars in magenta and cyan in Figure 15. Notice that in this case the SFRs are multiplied by 100.

much closer (1.62 Mpc) and allows its oldest stars to be detected. In fact, McQuinn et al. (2015) find that it indisputably contains stars as old as 10 Gyr. As a matter of fact, there is no evidence so far for the existence of a young galaxy in the Local Universe.

From a quantitative derivation of DDO 68's SFH based on the synthetic CMD method, we estimated that the mass locked up in old (age >1 Gyr) stars is $M_\star \simeq 1.0 \times 10^8\, M_\odot$, i.e., almost 80% of the total galaxy stellar mass. Obviously, the closer distance of DDO 68 compared to I Zw 18 (~12 Mpc versus ~18 Mpc)
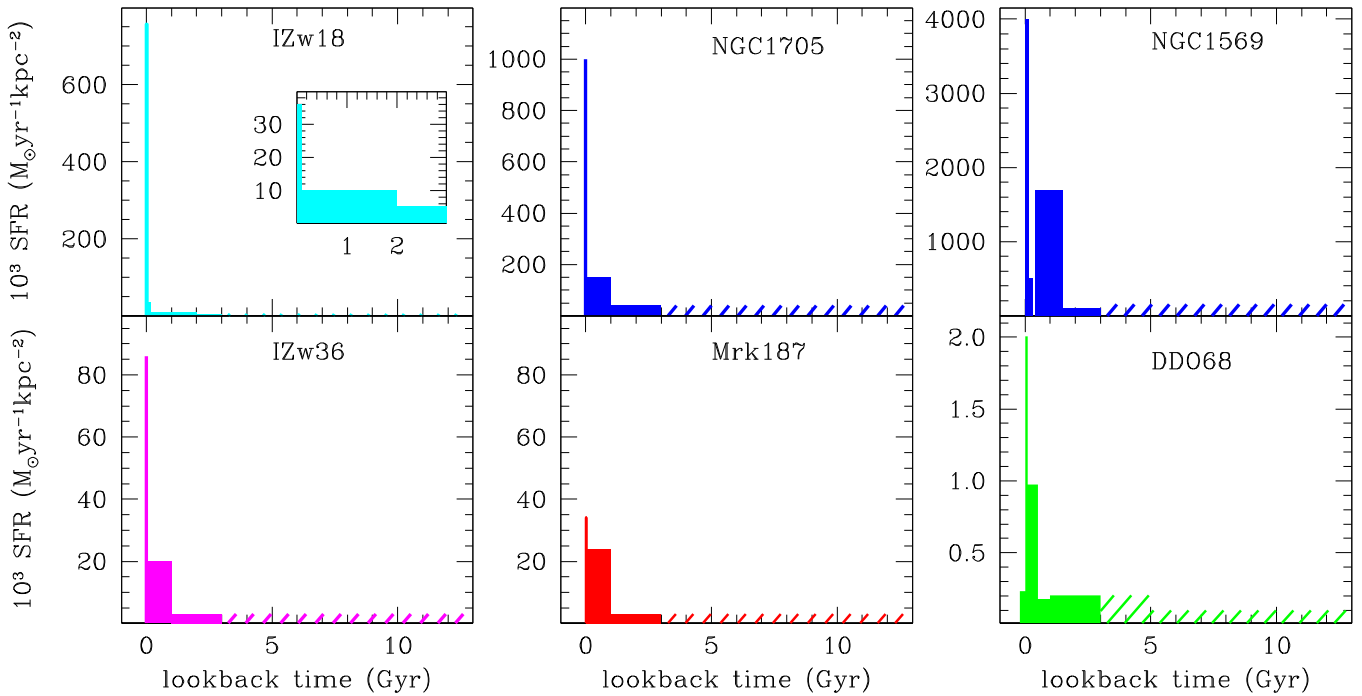
Figure 17. SFHs of BCDs and starburst dwarfs in the Local Volume. The SFR densities are all multiplied by 1000, but the scale of the ordinate varies from one panel to the other. The onset in the top-left panel provides a blow-up of the plot portion between 0 and 3 Gyr ago, barely visible in the main graph. The solid histograms show what we consider a robust SFH resulting from the assumption that RGB stars resolved in these low metallicity galaxies are at least 3 Gyr old. The shaded areas are only indicative of what is possibly the SFH at earlier epochs. Notice that for both NGC 1569 and NGC 1705 the plotted values result from the combination of two subsequent and consistent SFH derivations from the same group (see the text for references).

allowed us to better constrain the total stellar mass formed at these epochs. We consider this result quite robust, while the details on the SFH earlier than 1–2 Gyr, as well as the age of the onset of the SF, should be taken with caution, due to the degeneracy of the stellar models on the RGB and to the large photometric errors at the faintest magnitudes. We emphasize, however, that the low metallicity of DDO 68 mitigates the age–metallicity degeneracy and allows us to argue on safer grounds that the redder RGB stars are likely 10–13 Gyr old. On the other hand, the SFH derived at epochs younger than ∼1 Gyr offers a more realistic view of the recent SF activity in DDO 68. We derived an average SFR of $\simeq 7.1 \times 10^{-4}\ M_\odot\ \mathrm{yr}^{-1}\ \mathrm{kpc}^{-2}$ over the last ∼1 Gyr (we excluded Region 4 in this case because we want to estimate the average SFR over the main body, while Region 4 clearly includes the extremities and is the least well defined), which is typical of the majority of star-forming dwarf galaxies; the most recent SF activity is quite modest, and not even comparable to the burst strengths (see e.g., Tolstoy et al. 2009; Tosi 2009, and references therein) in "monsters" like NGC 1569 and NGC 1705.

Figure 17 shows the global SFR density (i.e., normalized to the area) of DDO 68 as a function of time, as derived for this paper, together with those of five other starburst dwarfs for which *HST* allowed us to derive the SFH within the look-back time given by the resolved RGB stars (formally >1 Gyr, but in all cases taken as ∼3 Gyr, thanks to the low metallicity of these galaxies, which significantly mitigates the age–metallicity degeneracy on the RGB). It is important to notice that at distances of a few Mpc the SFH older than 1 Gyr necessarily relies on RGB stars; therefore, the corresponding uncertainties are huge (see Appendix B of Weisz et al. 2011). Together with the mentioned NGC 1569 (Greggio et al. 1998; Angeretti et al. 2005) and NGC 1705 (Annibali et al. 2003, 2009), we

include in this comparison I Zw 18 (Annibali et al. 2013), I Zw 36 (Schulte-Ladbeck et al. 2001), and MrK 187 (Schulte-Ladbeck et al. 2000). The shown galaxies are too far away even to detect the He-burning phase of stars with ages between 0.5 and 1 Gyr, hence the resulting SFHs are rather uncertain also in that age range. However, within the uncertainties, the resulting scenario is correct. All these galaxies show a well defined very recent burst and moderate ancient SFRs, as old as the look-back time reached by the photometry, with no evidence for interruptions in the SF. Similar results are also found in other studies of dIrr galaxies (McQuinn et al. 2010; Weisz et al. 2011), which typically show a significant SF in the oldest epochs plus, in the case of starburst galaxies, elevated levels of recent SF. The details of the SFHs, however, can considerably vary from galaxy to galaxy.

Extremely metal-poor galaxies have recently been classified into two major groups, namely quiescent and active, in an attempt to understand their evolutionary stage and why they are so few (James et al. 2015). Quiescent ones (like Leo P) are numerous but very faint, and therefore remain undetected when at relatively large distances, whereas active ones (like I Zw 18) are undergoing a starburst and are easily detected even at large distances. DDO 68 is certainly not a starburst dwarf, but its level of star formation is high enough to let it be clearly recognizable in spite of its relatively large distance.

As with all studied star-forming dwarfs, DDO 68 does not show evidence of long interruptions in the SFH, with an overall activity more "gasping" than bursting; at all ages, the SFR density decreases from the center outwards. The distribution of the old stellar population is quite homogeneous and traces the whole galaxy, while young stars tend to be more concentrated. All of these characteristics make DDO 68 a "normal" star-forming dwarf galaxy.

Nonetheless, there are properties that make it exceptional: its highly disturbed morphology and the presence of an arc-shaped structure populated by stars of all ages, and rich in H II regions, is a very peculiar characteristic, which strongly suggests a merging/accretion scenario. Interestingly, a peak in the star formation activity between ∼30 and ∼50 Myr is found in all regions of DDO 68, suggesting that this epoch may have been affected by the interaction of two merging bodies. A merging event between DDO 68 and a possible companion could also explain why DDO 68 is an outlier in the mass–metallicity relation for dwarf star-forming galaxies, with a metallicity similar to that of I Zw 18, but with a stellar mass ∼10 times higher: the H II region abundances derived by Pustilnik et al. (2005) in the arc-shaped structure could in fact trace the metallicity of the accreted companion DDO 68 B, but not the (possibly higher) metallicity of DDO 68 A (Tikhonov et al. 2014). A merging event could also have triggered the recent SF observed at relatively large galactocentric distances (as demonstrated by our CMD analysis and by the presence of Hα emission), which is a quite uncommon feature. Finally, we recognized, in the RGB spatial map, a small concentration of stars toward the upper right edge of the ACS chip, noticed also by Tikhonov et al. (2014); in order to better investigate the nature of this feature, we obtained new wide-field imaging data at the LBT. These new data, together with preliminary results on the accretion history of DDO 68, are presented by Annibali et al. (2016).

DDO 68 is also part of the LEGUS (Legacy Extra Galactic UV Survey) program, which is an *HST* Treasury Program imaging 50 local (within ∼12 Mpc) galaxies with WFC3 and ACS with the goal of studying in detail the most recent SF, the effects of the SFH on the UV SFR calibrations, the impact of environment on the star formation, and the properties and the evolution of star clusters. Thanks to these new data, we will be able to explore the very recent SF in DDO 68 and to better understand what triggered its most recent SF activity.

REFERENCES

Aloisi, A., Clementini, G., Tosi, M., et al. 2007, ApJL, 667, L151
Anderson, J., & Bedin, L. R. 2010, PASP, 122, 1035
Angeretti, L., Tosi, M., Greggio, L., et al. 2005, AJ, 129, 2203
Annibali, F., Cignoni, M., Tosi, M., et al. 2013, AJ, 146, 144
Annibali, F., Greggio, L., Tosi, M., Aloisi, A., & Leitherer, C. 2003, AJ, 126, 2752
Annibali, F., Nipoti, C., Ciotti, L., et al. 2016, ApJ, 826, 27
Annibali, F., Tosi, M., Aloisi, A., van der Marel, R. P., & Martinez-Delgado, D. 2012, ApJL, 745, L1
Annibali, F., Tosi, M., Monelli, M., et al. 2009, AJ, 138, 169
Bellazzini, M., Ferraro, F. R., Sollima, A., Pancino, E., & Origlia, L. 2004, A&A, 424, 199
Berg, D. A., Skillman, E. D., Marble, A. R., et al. 2012, ApJ, 754, 98
Bohlin, R. C. 2012, Flux Calibration of the ACS CCD Cameras IV Absolute Fluxes, Tech. Rep.
Bressan, A., Marigo, P., Girardi, L., et al. 2012, MNRAS, 427, 127
Caffau, E., Ludwig, H.-G., Steffen, M., et al. 2008, A&A, 488, 1031
Cannon, J. M., Johnson, M., McQuinn, K. B. W., et al. 2014, ApJL, 787, L1
Cignoni, M., Sabbi, E., van der Marel, R. P., et al. 2015, ApJ, 811, 76
Cioni, M.-R. L., van der Marel, R. P., Loup, C., & Habing, H. J. 2000, A&A, 359, 601
Dolphin, A. E. 2013, ApJ, 775, 76
Fruchter, A. S., Hack, W., Droetboom, M., et al. 2009, in Bulletin of the American Astronomical Society 213, American Astronomical Society Meeting Abstracts, Vol. 41, 467.02
Giovanelli, R., Haynes, M. P., Adams, E. A. K., et al. 2013, AJ, 146, 15
Gottlöber, S., Łokas, E. L., Klypin, A., & Hoffman, Y. 2003, MNRAS, 344, 715
Greggio, L., Tosi, M., Clampin, M., et al. 1998, ApJ, 504, 725
Grocholski, A. J., van der Marel, R. P., Aloisi, A., et al. 2012, AJ, 143, 117
Hoeft, M., Yepes, G., Gottlöber, S., & Springel, V. 2006, MNRAS, 371, 401
Izotov, Y. I., & Thuan, T. X. 1999, ApJ, 511, 639
Izotov, Y. I., & Thuan, T. X. 2002, ApJ, 567, 875
Izotov, Y. I., & Thuan, T. X. 2004, ApJ, 616, 768
Izotov, Y. I., & Thuan, T. X. 2009, ApJ, 690, 1797
James, B. L., Koposov, S., Stark, D. P., et al. 2015, MNRAS, 448, 2687
Kroupa, P. 2001, MNRAS, 322, 231
Leitherer, C., Schaerer, D., Goldader, J. D., et al. 1999, ApJS, 123, 3
McQuinn, K. B. W., Skillman, E. D., Cannon, J. M., et al. 2010, ApJ, 721, 297
McQuinn, K. B. W., Skillman, E. D., Dolphin, A., et al. 2015, ApJ, 812, 158
Meynet, G., & Maeder, A. 2002, A&A, 390, 561
Mighell, K. J. 1999, ApJ, 518, 380
Peebles, P. J. E. 2001, ApJ, 557, 495
Pustilnik, S. A., Kniazev, A. Y., & Pramskij, A. G. 2005, A&A, 443, 91
Pustilnik, S. A., & Tepliakova, A. L. 2011, MNRAS, 415, 1188
Pustilnik, S. A., Tepliakova, A. L., & Kniazev, A. Y. 2008, AstL, 34, 457
Rojas, R. R., Vogeley, M. S., Hoyle, F., & Brinkmann, J. 2004, ApJ, 617, 50
Rojas, R. R., Vogeley, M. S., Hoyle, F., & Brinkmann, J. 2005, ApJ, 624, 571
Schlegel, D. J., Finkbeiner, D. P., & Davis, M. 1998, ApJ, 500, 525
Schulte-Ladbeck, R. E., Hopp, U., Drozdovsky, I. O., Greggio, L., & Crone, M. M. 2002, AJ, 124, 896
Schulte-Ladbeck, R. E., Hopp, U., Greggio, L., & Crone, M. M. 2000, AJ, 120, 1713
Schulte-Ladbeck, R. E., Hopp, U., Greggio, L., Crone, M. M., & Drozdovsky, I. O. 2001, AJ, 121, 3007
Sirianni, M., Jee, M. J., Benítez, N., et al. 2005, PASP, 117, 1049
Skillman, E. D., & Kennicutt, R. C., Jr. 1993, ApJ, 411, 655
Skillman, E. D., Salzer, J. J., Berg, D. A., et al. 2013, AJ, 146, 3
Stetson, P. B. 1987, PASP, 99, 191
Stil, J. M., & Israel, F. P. 2002a, A&A, 389, 29
Stil, J. M., & Israel, F. P. 2002b, A&A, 389, 42
Tikhonov, N. A., Galazutdinova, O. A., & Lebedev, V. S. 2014, AstL, 40, 1
Tolstoy, E., Gallagher, J. S., Cole, A. A., et al. 1998, AJ, 116, 1244
Tolstoy, E., Hill, V., & Tosi, M. 2009, ARA&A, 47, 371
Tosi, M. 2009, in IAU Symp. 258, The Ages of Stars, ed. E. E. Mamajek, D. R. Soderblom, & R. F. G. Wyse (Cambridge Univ. Press), 61
Tosi, M., Greggio, L., Marconi, G., & Focardi, P. 1991, AJ, 102, 951
Weisz, D. R., Dalcanton, J. J., Williams, B. F., et al. 2011, ApJ, 739, 5